Ionic Mechanisms Underlying Bistability in Spinal Motoneurons: Insights from a Computational Model

Yaroslav I. Molkov,[1,2,#] Florent Krust,[3,&] Russell Jeter,[1,2,&] Tommy Stell,[1] Mohammed A. Y. Mohammed,[1] Frédéric Brocard,[3,$] Ilya A. Rybak[4,$]

[1] Department of Mathematics and Statistics, Georgia State University, Atlanta, GA, USA
[2] Neuroscience Institute, Georgia State University, Atlanta, GA, USA
[3] Institut de Neurosciences de la Timone, Aix Marseille University, CNRS, Marseille, France
[4] Department of Neurobiology and Anatomy, Drexel University College of Medicine, Philadelphia, PA, USA

[#] Corresponding Author: email: ymolkov@gsu.edu

[&] There authors contributed equally

[$] Shared senior authorship

Key Points

- We investigated how spinal motoneurons, critical for skeletal muscle control, exhibit bistability, switching between quiet and self-sustained firing. This property stabilizes motor functions like postural control, and its dysregulation contributes to disorders such as spasticity. Using a single-compartment computational model and mouse spinal slice recordings, we explored the ionic interactions driving bistability.
- Our findings reveal that a calcium-activated cation non-specific current and calcium-induced calcium release form a core mechanism supporting the plateau depolarization essential for bistable firing. Within this framework, the persistent sodium current facilitates plateau generation, while the calcium-dependent potassium current counteracts it. Pharmacological manipulations in slices yielded results consistent with these current roles.
- Our study delineates the ionic dependencies of motoneuron bistability based on interactions, not spatial location. This offers a concise framework for interpreting excitability changes observed in normal conditions and following spinal cord injury, providing valuable insights into motor function and neurological disorders.

Abstract

Spinal motoneurons are the final output of spinal circuits that engage skeletal muscles to generate motor behaviors. Many motoneurons exhibit bistable behavior, alternating between a quiescent resting state and a self-sustained firing mode, classically attributed to plateau potentials driven by persistent inward currents. This intrinsic property is important for normal movement control, but can become dysregulated, causing motor function deficits, like spasticity. Here we use a conductance-based single-compartment model, together with mouse spinal slice recordings,to investigate the ionic interactions underlying motoneuron bistability. We show that synergistic interactions among high-voltage-activated L-type Ca^{2+} current (I_{CaL}), calcium-induced calcium release (CICR) and the Ca^{2+}-activated non-specific cation current (I_{CAN}) constitute a minimal mechanistic core that produces plateau potentials and bistable firing. Within this framework, the persistent sodium current (I_{NaP}) promotes plateau generation, in contrast to the Ca^{2+}-dependent K^+ current (I_{KCa}) which opposes it. These results delineate ionic dependencies at the level of interactions rather than spatial localisation and provide a tractable basis for interpreting altered motoneuron excitability in disease.

Introduction

Motoneurons show a variety of nonlinear intrinsic behaviors that determine their input-output properties (Binder et al., 2020). Among them, bistability allows motoneurons to toggle between two stable states: a quiescent resting state, and a self-sustained firing state characterized by a regular pattern of action potentials generated in absence of synaptic drive. A short excitatory input can trigger a transition from the quiescent state to the active state, whereas a brief inhibitory input can induce the opposite transition (Hultborn et al., 1975; Hounsgaard et al., 1984). The underlying mechanism of the bistability involves formation of plateau potentials, long-lasting membrane depolarizations, during which the motoneuron firing is maintained (Hounsgaard, Hultborn, et al., 1988; Hounsgaard & Mintz, 1988). Persistent firing described in motor units in intact animals (Eken et al., 1989; Eken & Kiehn, 1989; Kiehn & Eken, 1997) as well as in humans (M. A. Gorassini et al., 1998; M. Gorassini et al., 1999; Collins et al., 2001) provides indirect evidence that motoneuron bistability is an important feature of motor control contributing to many behaviors. It has been suggested that bistability is involved in postural control lessening the requirement for continuous synaptic drive (Hounsgaard, Hultborn, et al., 1988; Lee & Heckman, 1998a; Heckman et al., 2009). Consistent with this, limiting motoneuron bistability was shown to impair postural control (Bos et al., 2021).

Early studies proposed that bistability primarily resulted from a persistent component of the calcium current (I_{CaL}) (Hounsgaard & Mintz, 1988; Hounsgaard & Kiehn, 1989) conducted through Cav1.3 channels (Carlin et al., 2000; Simon et al., 2003; Zhang et al., 2006). However, subsequent research has shown that bistability results from a more complex interaction of several ionic currents (Bouhadfane et al., 2013), including the calcium-activated non-specific cation current (I_{CAN}) through the Transient Receptor Potential Melastatin 5 (TRPM5) channels (Bos et al., 2021) and the persistent sodium current (I_{NaP}) via Nav1.6 channels (Drouillas et al.,

2023). The emerging picture is a causal sequence of cellular processes: the initial membrane depolarization activates I_{NaP}, triggering firing and calcium influx; I_{CaL} increases intracellular calcium, which then activates calcium-induced calcium release (CICR) and recruits I_{CAN}, leading to further depolarizing of the membrane. This cascade of depolarization and triggered currents leads to self-sustained firing, reinforcing the positive feedback loop underlying bistability. The contribution of these intrinsic processes to motoneuron bistability is closely tied to cell size with larger motoneurons exhibiting both higher current expression and a greater propensity for bistable behavior (Harris-Warrick et al., 2024).

Bistability is modulated by neuromodulatory and biophysical contexts. Monoamines released from supraspinal centers can promote and unmask bistability in motoneurons with its latent or partial expression (Conway et al., 1988; Hounsgaard, Hultborn, et al., 1988; Hounsgaard & Kiehn, 1989; Perrier & Delgado-Lezama, 2005). Temperature also modulates bistability: values above 30°C unmask plateau potentials by recruiting thermosensitive currents mediated by TRPM5 channels (Bos et al., 2021).

Beyond its physiological role, bistability has critical implications in pathology. Following spinal cord injury, excessive bistability in motoneurones has been linked to spasticity, a disabling condition characterized by involuntary muscle contractions (Bennett et al., 2001; Heckman et al., 2008) arising from dysregulated intrinsic ionic currents that amplify self-sustained firing and disrupt motor control (C. Brocard et al., 2016; Murray et al., 2010).

Despite significant progress, our understanding of multiple ionic mechanisms underlying bistability remains incomplete. Prior studies often examined the roles of single currents in isolation, leaving open the possible importance of their integration and interactions for motoneuron excitability. In this study, we combine computational modeling, using a conductance-based single-compartment motoneuron model, with mouse spinal slice recordings to dissect how these currents, considered separately and in combination, control the emergence, maintenance and modulation of bistability in motoneurons. Our goal is to identify a minimal mechanistic core of motoneuron bistability at the level of ionic interactions.

Methods

Modeling methods

Motoneuron model

We used a conductance-based single-compartment mathematical model of a motoneuron that includes the main spike-generating channels, fast sodium (I_{NaF}) and potassium rectifier (I_{Kdr}), as well as the persistent sodium (I_{NaP}), slowly inactivating potassium ($I_{Kv1.2}$), high-voltage activated calcium (I_{CaL}), Ca^{2+}-activated, non-specific cation (I_{CAN}, associated with TRPM5 channels) and Ca^{2+}-dependent potassium (I_{KCa}, associated with SK channels) current.

The voltage dynamics are described by the current balance equation:

$$C \cdot \frac{dV}{dt} = - I_{NaF} - I_{NaP} - I_{Kdr} - I_{Kv1.2} - I_{CaL} - I_{KCa} - I_{CAN} - I_L + I_{inj}, \qquad (1)$$

where V is membrane potential in mV, t is time in ms, C is membrane capacitance $\left(C = 1\ \mu F \cdot cm^{-2}\right)$, and the right hand side of the equation contains all transmembrane currents described as follows.

Fast sodium current (Booth et al., 1997):

$$I_{NaF} = g_{NaF} \cdot m_{NaF}(V)^3 \cdot h_{NaF}(V) \cdot (V - E_{Na});$$

$$m_{NaF}(V) = (1 + \exp(-(V + 35)/7.8))^{-1};$$

$$\tau_{NaF}(V) \cdot \frac{dh_{NaF}}{dt} = h_{NaF\infty}(V) - h_{NaF};$$

$$\tau_{NaF}(V) = 30 \cdot (\exp((V + 50)/15) + \exp(-(V + 50)/16))^{-1};$$

$$h_{NaF\infty}(V) = (1 + \exp((V + 55)/7))^{-1},$$

$$g_{NaF} = 120\ mS/cm^2,\ E_{Na} = 55\ mV.$$

The persistent sodium current was assumed to be non-inactivating. Activation was assumed instantaneous and non-inactivating. Activation dependence on voltage was taken from (F. Brocard et al., 2013), :

$$I_{NaP} = g_{NaP} \cdot m_{NaP}(V) \cdot h_{NaP}(V) \cdot (V - E_{Na});$$

$$m_{NaP}(V) = (1 + \exp(-(V + 53)/3))^{-1};$$

Persistent sodium current is assumed non-inactivating, i.e. $h_{NaP}(V) = 1$.

Potassium rectifier current (Booth et al., 1997):

$$I_{Kdr} = g_{Kdr} \cdot m_{Kdr}(V)^4 \cdot (V - E_K);$$

$$\tau_{Kdr}(V) \cdot \frac{dm_{Kdr}}{dt} = m_{Kdr\infty}(V) - m_{Kdr};$$

$$\tau_{Kdr}(V) = 7 \cdot (\exp((V + 40)/40) + \exp(-(V + 40)/50))^{-1};$$

$$m_{Kdr\infty}(V) = (1 + \exp(-(V + 28)/15))^{-1};$$

$$g_{Kdr} = 100\, mS/cm^2,\ E_K = 26.54 \cdot \log([K^+]_o/[K^+]_i),\ [K^+]_i = 140\, mM,\ [K^+]_o \in [4, 12]\, mM.$$

Slowly inactivating potassium current (Bos et al., 2018):

$$I_{Kv1.2} = g_{Kv1.2} \cdot m_{Kv1.2}(V) \cdot h_{Kv1.2}(V) \cdot (V - E_K);$$

$$\tau^x_{Kv1.2}(V) \cdot \frac{dx_{Kv1.2}}{dt} = x_{Kv1.2\infty}(V) - x_{Kv1.2},\ x \in \{m, h\};$$

$$\tau^m_{Kv1.2}(V) = 2.44 + 18.387 \cdot (\exp(-(V - 25.645)/21.633) + \exp((V + 4.42)/45.9))^{-1};$$

$$m_{Kv1.2\infty}(V) = (1 + \exp(-(V + 46)/6.9))^{-1};$$

$$\tau^h_{Kv1.2}(V) = 74.74 \cdot (0.00015 \cdot \exp(-(V + 13)/15) + 0.06 \cdot (1 + \exp(-(V + 68)/12))^{-1})^{-1};$$

$$h_{Kv1.2\infty}(V) = (1 + \exp((V + 54)/7.1))^{-1};$$

$$g_{Kv1.2} \in [0, 10]\, mM.$$

High-voltage calcium *L* (I_{CaL}) current (Jasinski et al., 2013):

$$I_{CaL} = g_{CaL} \cdot m_{CaL}(V) \cdot h_{CaL}(V) \cdot (V - E_{Ca});$$

$$\tau^x_{CaL} \cdot \frac{dx_{CaL}}{dt} = x_{CaL\infty}(V) - x_{CaL},\ x \in \{m, h\};$$

$$m_{CaL\infty}(V) = (1 + \exp(-(V + 27.5)/5.7))^{-1};$$

$$h_{CaL\infty}(V) = (1 + \exp((V + 52.4)/5.2))^{-1};$$

$$E_{Ca} = 80\, mV,\ g_{CaL} = 0.05\, mS/cm^2,\ \tau^m_{CaL} = 0.5\, ms,\ \tau^h_{CaL} = 18\, ms.$$

Calcium-activated nonspecific cation (I_{CAN}) current (Toporikova & Butera, 2011):

$$I_{CAN} = g_{CAN} \cdot \frac{Ca}{Ca + K_{CAN}} \cdot (V - E_{CAN}),\ K_{CAN} = 0.74 \cdot 10^{-3}\, mM,\ E_{CAN} = 0\, mV.$$

Calcium-dependent potassium current (I_{KCa}) (Booth et al., 1997). This current was modified to be instantaneous:

$$I_{KCa} = g_{KCa} \cdot \frac{Ca}{Ca+K_d} \cdot (V - E_K),\ K_d = 0.2 \cdot 10^{-3}\ mM.$$

Leak current:

$$I_L = g_L \cdot (V - E_L),\ g_L = 0.1\ mS/cm^2,\ E_L = -80\ mV.$$

The two currents described above (I_{CAN} and I_{KCa}) depend on the intracellular Ca^{2+} concentration $[Ca^{2+}]_i$ in mM (denoted by Ca in the equations). The Ca^{2+} concentration increases directly from the influx of calcium ions through calcium channels (captured by I_{CaL} in the mathematical model) and indirectly from the release of calcium ions from intracellular stores via a calcium-induced calcium release (CICR) mechanism. Additionally, they are pumped out by the Ca-ATP pumps.

The dynamics of intracellular calcium concentration (*Ca*) in our model are described by the differential equation:

$$\frac{dCa}{dt} = -f \cdot \alpha \cdot I_{CaL} + k_{CICR} \cdot Ca - Ca/\tau_{Ca}. \qquad (2)$$

On the right hand side of this equation, the first term represents calcium influx through high-threshold, voltage-gated calcium channels (I_{CaL}) which open during action potentials. Here $f = 0.01$ defines the ratio of entered Ca^{2+} ions remaining unbound; the coefficient $\alpha = (2 \cdot F \cdot \delta)^{-1}$ converts inward I_{CaL} current to Ca^{2+} concentration rate of change; here F is Faraday's constant ($F = 9.648 \cdot 10^4\ C/mol$) and δ is the thickness ($0.1\ \mu m$) of the shell adjacent to the membrane. Based on these parameters, $\alpha = 5 \cdot 10^{-4}\ mM \cdot cm^2 \cdot ms^{-1} \cdot \mu A^{-1}$.

The second term describes an increase of cytoplasmic Ca^{2+} concentration through the CICR mechanism, where the rate of calcium release from internal stores is proportional to the intracellular Ca^{2+} concentration (defined by k_{CICR}). The third term describes the action of calcium pumps (both plasma membrane and SERCA) which rapidly remove calcium from the cytoplasm, with a time constant $\tau_{Ca} = 10\ ms$.

Qualitative analysis

To investigate the bistable behavior of spinal motoneurons, we implemented a current ramp simulation protocol designed to probe the transitions between quiescent and self-sustained firing states. This approach leverages a linearly varying injected current (I_{inj}) to systematically explore the system's response across a range of input intensities, making it an effective tool for detecting hysteresis and state-dependent dynamics in neuronal models.

The protocol was designed as follows: the injected current was initially set to zero and then increased linearly to a predetermined maximum value (ascending phase) over a specified duration. Subsequently, the current was decreased linearly back to zero (descending phase) at the same rate. This bidirectional ramp allowed us to identify two key transition points: the

current threshold at which the system shifts from silence to spiking during the ascending phase (I_{up}) and the lower threshold at which spiking ceases during the descending phase (I_{down}). Bistability is indicated when I_{down} is less than I_{up}, revealing a range of current values where the system can stably maintain either state, depending on its prior condition. This hysteresis reflects the nonlinear properties of the model and its history-dependent behavior. To ensure the reliability of these thresholds, the ramp time was varied systematically, extending the duration of the ascending and descending phases until I_{up} and I_{down} stabilized, confirming that the observed transitions were not influenced by transient dynamics. Typically, ramp durations spanned several hundred milliseconds, with longer durations tested to exclude such effects.

To further validate the protocol's ability to detect bistability, we employed a complementary current step simulation inspired by experimental approaches. Starting from a baseline of $I_{inj} = 0$, the current was stepped to an intermediate value within the suspected bistable range ($I_{down} < I_{inj} < I_{up}$), then increased to a level above I_{up}, and subsequently returned to the intermediate value before returning to zero. This sequence demonstrated that, at the intermediate current level, the system's state—silent or spiking—depended on its prior activation history, reinforcing the findings of the ramp protocol.

The current ramp simulations also supported parametric analyses by varying key model parameters and plotting the resulting bifurcation diagrams. These diagrams mapped the system's equilibrium points and oscillatory regimes as functions of I_{inj}, providing a visual representation of the bistable region. The protocol's design, with its carefully adjusted ramp duration, ensured that the gradual variation of input current effectively captured the boundaries of this region, offering a robust technical framework for studying the conditions under which bistability emerges and persists in the model.

Simulations

Simulations were performed using custom-written C++ and Julia software. Integration was performed by the Dormand-Prince 5(4) method using (*Boost C++ Libraries*, ver. 1.86). Source code written in C++ and Julia for the model and examples of the ramping protocols can be found in the Github repository associated with this manuscript (Jeter & Molkov, 2025).

Experimental methods

Experimental model

Mice (C57/Bl6 background) were housed under a 12h light/dark cycle with *ad libitum* access to water and food. Room temperature was kept between 21-24°C and between 40-60% relative humidity. All animal care and use were conformed to the French regulations (Décret 2010-118) and approved by the local ethics committee (Comité d'Ethique en Neurosciences INT-Marseille, CE71 Nb A1301404, authorization Nb 2018110819197361).

In vitro preparations

For the slice preparation, the lumbar spinal cord was isolated in ice-cold (+4°C) artificial CSF (aCSF) solution composed of the following (in mM): 252 sucrose, 3 KCl, 1.25 KH_2PO_4, 4 $MgSO_4$, 0.2 $CaCl_2$, 26 $NaHCO_3$, 25 D-glucose, pH 7.4. The lumbar spinal cord was then introduced into a 1% agar solution, quickly cooled, mounted in a vibrating microtome (Leica, VT1000S) and sliced (325 µm) through the L4–5 lumbar segments. Slices were immediately transferred into the holding chamber filled with bubbled (95% O_2 and 5% CO_2) aCSF solution composed of (in mM): 120 NaCl, 3 KCl, 1.25 NaH_2PO_4, 1.3 $MgSO_4$, 1.2 $CaCl_2$, 25 $NaHCO_3$, 20 D-glucose, pH 7.4, 30-32°C. After a 30-60 min resting period, individual slices were transferred to a recording chamber continuously perfused with aCSF heated to 32-34°C.

In vitro recordings

Whole-cell patch-clamp recordings were performed using a Multiclamp 700B amplifier (Molecular Devices) from L4-L5 motoneurons with the largest soma (>400µm2) located in the lateral ventral horn. Patch electrodes (2-4 MΩ) were pulled from borosilicate glass capillaries (1.5 mm OD, 1.12 mm ID; World Precision Instruments) on a Sutter P-97 puller (Sutter Instruments Company) and filled with an intracellular solution (in mM): 140 K^+-gluconate, 5 NaCl, 2 $MgCl_2$, 10 HEPES, 0.5 EGTA, 2 ATP, 0.4 GTP, pH 7.3. Pipette and neuronal capacitive currents were canceled and, after breakthrough, the series resistance was compensated and monitored. Recordings were digitized on-line and filtered at 20 kHz through a Digidata 1550B interface using Clampex 10.7 software (Molecular Devices). All experiments were designed to gather data within a stable period (i.e., at least 2 min after establishing whole-cell access).

Data quantification

Electrophysiological data analyses were analyzed off-line with Clampfit 10.7 software (Molecular Devices). For intracellular recordings, several basic criteria were set to ensure optimum quality of intracellular recordings. Only cells exhibiting a stable resting membrane potential, access resistance (no > 20% variation) and an action potential amplitude larger than 40 mV under normal aCSF were considered. Passive membrane properties of cells were measured by determining from the holding potential the largest voltage deflections induced by small current pulses that avoided activation of voltage-sensitive currents. We determined input resistance by the slope of linear fits to voltage responses evoked by small positive and negative current injections. The peak amplitude of the slow afterdepolarization (slow ADP or sADP) was defined as the difference between the holding potential and the peak voltage deflection after the burst of spikes. The sADP area was measured between the end of the stimulus pulse and the onset of the hyperpolarizing pulse (delta= 7.5 s). In addition, the duration of the sADP was quantified as the time interval at half-maximal amplitude. If necessary, using bias currents, the pre-pulse membrane potential was maintained at the holding potential fixed in the control condition. Bistable properties were investigated with a 2 s depolarizing current pulses of varying amplitudes (0.8 - 2 nA). To quantify the ability of a motoneuron to be bistable, we gradually increased the holding current in 25 pA steps over a 2-second period before delivering the

depolarizing pulse. This process continued until the neuron reached its spiking threshold. The cell was considered as bistable when (1) the pre-stimulus membrane potential stays relatively hyperpolarized below the spiking threshold (downstate), (2) the post-stimulus membrane potential stays depolarized above the spike threshold (upstate), and (3) the membrane potential switches to downstate after a brief hyperpolarizing pulse. To quantify the extent of bistability, we measured both the voltage (*V*) range between the most hyperpolarized holding potential (*Vh min*) and the most depolarized holding potential (*Vh max)* at which the motoneuron can exhibit a self-sustained spiking, and the corresponding range of injected currents (*I*) over which bistable behavior was observed.

Statistics

When two conditions (control vs drugs) were compared, we used the Wilcoxon matched pairs test. For all statistical analyses, the data met the assumptions of the test and the variance between the statistically compared groups was similar. The level of significance was set at $p < 0.05$. Statistical analyses were performed using Graphpad Prism 7 software.

Results

Calcium dynamics and calcium-dependent currents

The role of calcium-induced calcium release (CICR) mechanism

A brief excitatory current pulse into a motoneuron triggers a train of action potentials, causing a substantial increase in intracellular calcium levels ($[Ca^{2+}]_i$). This increase is driven by influx via voltage-gated calcium channels, further amplified by calcium-induced calcium release (CICR) from internal stores. The resulting $[Ca^{2+}]_i$ accumulation activates two Ca^{2+}-dependent currents with opposing effects: the depolarizing calcium-activated nonspecific cation current (I_{CAN}) and the hyperpolarizing calcium-dependent potassium current (I_{KCa}).

As described in Methods, the $[Ca^{2+}]_i$ dynamics in our model are governed by the differential equation (2). The calcium clearance pump operates with a time constant of $\tau_{Ca} = 10$ ms, which, in the absence of CICR, would clear all calcium introduced by a spike before the next spike. The term $k_{CICR} \cdot Ca$ in equation (2) captures the CICR mechanism, where the rate of calcium release from internal stores is directly proportional to the current calcium concentration Ca with coefficient k_{CICR}.

For simplicity, the intracellular calcium dynamics described by Eq. (2) can be expressed as:

$$\frac{dCa}{dt} = - f \cdot \alpha \cdot I_{CaL} - Ca/\tau_{eff},$$

where τ_{eff} represents the effective time constant

$$\tau_{eff} = (1/\tau_{Ca} - k_{CICR})^{-1}.$$

The gain k_{CICR} must not exceed $1/\tau_{Ca}$ to prevent negative τ_{eff}, which would lead to an infinite increase in calcium. In our model, k_{CICR} is set at 0.096 ms^{-1}, yielding an effective time constant $\tau_{eff} = 250$ ms. This value was chosen phenomenologically to match typical slow afterdepolarization decay rates observed in our *in vitro* data and prior studies.

This prolonged τ_{eff} (compared to τ_{Ca}) reflects how the CICR mechanism substantially slows calcium clearance, resulting in $[Ca^{2+}]_i$ build-up during repetitive firing. As shown in Figure 1, calcium levels sharply increase in response to a rectangular current pulse, strongly activating I_{CAN} and I_{KCa}. Without CICR (k_{CICR} = 0), pumps clear calcium rapidly between spikes, preventing significant accumulation during repetitive firing. Consequently, in the absence of sustained elevations in intracellular Ca^{2+} , neither I_{CAN} nor I_{KCa} currents are activated to a significant degree.

Interplay between I_{CAN} and I_{KCa}: afterdepolarization versus afterhyperpolarization

Intracellular recordings have shown that motoneurons demonstrate two post-stimulus behaviours: a slow afterdepolarization (sADP) after brief excitatory inputs, typical for a bistable motoneuron type, and an afterhyperpolarization (AHP) observed in a non-bistable motoneuron type (Harris-Warrick et al., 2024). Our model captures both behaviors and links them to the relative contributions of I_{CAN} and I_{KCa}. We also show that these currents have opposite effects on motoneuron bistability. When I_{KCa} predominates, Ca^{2+} -dependent potassium efflux produces hyperpolarization of the membrane and a decrease in excitability. This effect promotes spike-frequency adaptation and a prominent post-stimulus AHP supported by sustained $[Ca^{2+}]_i$ elevation (Fig. 1A).

Conversely, when I_{CAN} predominates, the elevation of $[Ca^{2+}]_i$ activates this current, leading to a depolarizing influx of sodium, that in turn increases the firing frequency during the pulse and yields an sADP afterward (Fig. 1B). As $[Ca^{2+}]_i$ declines, the membrane potential slowly relaxes back toward its resting values. These model behaviours are consistent with recordings and provide a mechanistic interpretation: I_{CAN} biases toward sADP and plateau maintenance, whereas I_{KCa} biases toward AHP and termination of spiking.

Mechanisms of I_{CAN}-based bistability and its modulation

I_{CAN}-based bistability

Our model predicts that the expression of I_{CAN} provides a robust route to bistability. The process begins with the opening of voltage-gated calcium channels during each action potential. While

this influx alone is insufficient to fully activate I_{CAN}, it triggers CICR, which amplifies $[Ca^{2+}]_i$ (see below).

The elevated $[Ca^{2+}]_i$ activates I_{CAN} establishing a positive feedback loop: I_{CAN} sustains depolarization, promoting continuous firing; spikes further elevate $[Ca^{2+}]_i$ via Ca^{2+} entry and CICR, and thus reinforce I_{CAN} activation. This self-perpetuating mechanism allows the motoneuron to remain in a high-activity state (persistent spiking) even after the initial stimulus is removed, creating bistability: the neuron can operate in either a quiescent state or an active spiking state.

To validate this mechanism, we replicated the experimental ramp current protocol in the model (see Methods). At g_{CAN} = 0.5 mS/cm^2 the voltage–current relation during a linear I_{inj} ramp (Fig. 2C) reveals distinct up and down thresholds. For $I_{inj} < I_{up}$ = 1.7 $\mu A/cm^2$, the system displays two attracting regimes separated by an unstable equilibrium (saddle): a stable hyperpolarized state corresponding to the resting state (silent) and a stable spiking state (limit cycle) (Fig. 2C). As I_{inj} exceeds I_{up} = 1.7 $\mu A/cm^2$, the low potential stable branch of the *V*-nullcline merges with the saddle and vanishes via a fold bifurcation, and the system transitions to a stable limit cycle representing a repetitive spiking regime. During the descending phase of the ramp, spiking persists until I_{inj} decreases to I_{down} = 1.1 $\mu A/cm^2$, which is less than I_{up} (Figs. 2C, D), yielding a hysteresis interval ($I_{down} < I_{inj} < I_{up}$), indicative of bistability.

To further probe bistability, we implemented a step protocol inspired by experimental methods. Starting at I_{inj} = 0 in a silent state, we applied an intermediate pulse within the bistable range ($I_{down} < I_{inj} < I_{up}$), then increased it above I_{up} to induce firing, before returning to the intermediate current (Fig. 2E). This protocol showed that, at the same intermediate current value, the motoneuron could either continue firing or remain silent, depending on whether it was previously activated.

The 2-parameter bifurcation diagram (Fig. 2A) shows how I_{CAN} controls the extent of the bistability region. At g_{CAN} = 0, I_{down} and I_{up} coincide (no hysteresis; Fig. 2B). Once g_{CAN} becomes large enough, the interval ($I_{down} < I_{inj} < I_{up}$) opens and bistability emerges. This is evident as the current required to trigger spiking during the ramp-up exceeds the current at which spiking stops during ramp-down (Fig. 2C). This hysteresis widens with further increases in g_{CAN} (Fig. 2A), reflecting the strengthening of the I_{CAN}-mediated positive feedback loop, which supports the self-sustained spiking state. These findings identify I_{CAN} as a key determinant of the bistable behavior.

The role of CICR

The model demonstrates that Ca^{2+} influx through voltage-gated calcium channels alone does not raise $[Ca^{2+}]_i$ enough to activate I_{CAN}. To illustrate the contribution of CICR we set k_{CICR} to 0, which reduces the effective decay time constant τ_{eff} to $\tau_{Ca} = 10\ ms$. As shown in Fig. 2F, the transient $[Ca^{2+}]_i$ increase is then sharply curtailed, I_{CAN} remains weak, and the I_{CAN}-based

bistability collapses (ramp hysteresis vanishes). In other words, CICR effectively slows Ca^{2+} clearance (τ_{eff} in the hundreds of ms) and is necessary in this framework to maintain the Ca^{2+}-dependent depolarizing drive provided by I_{CAN}.

The role of I_{KCa} in modulating I_{CAN}-based bistability

Our model indicates that I_{KCa} has a negative effect on I_{CAN}-based bistability. As $[Ca^{2+}]_i$ increases, SK-type K^+ channels (mediating I_{KCa}) open, allowing intracellular K^+ ions to exit the cell. This outward current hyperpolarizes the membrane, decreasing excitability, and preventing the self-sustaining depolarization provided by I_{CAN}. Bifurcation analyses (Fig. 3) summarize this interplay. At low g_{CAN}, a regime where I_{KCa} dominates the Ca^{2+}-dependent response, the neuron transitions between spiking and silence at the same current threshold during ascending and descending current ramps, with this common threshold only weakly influenced by g_{CAN} (Fig. 3A). Increasing g_{CAN} lowers the spiking onset threshold and, once g_{CAN} reaches approximately 1 mS/cm^2 (Fig. 3A), a hysteresis interval ($I_{down} < I_{inj} < I_{up}$) opens, indicating the emerging bistability. This is evident as the current required to trigger spiking during the ramp-up exceeds the current at which spiking stops during ramp-down, with the bistability range widening as g_{CAN} increases further. Additionally, the specific g_{CAN} value at which this bifurcation occurs depends linearly on g_{KCa} (Fig. 3B), suggesting that the bistability arises when I_{CAN} begins to dominate over I_{KCa}. Equivalently, reducing g_{KCa} at fixed g_{CAN} unmasks bistability (Figs. 3C-F).

We tested these predictions by performing patch-clamp recordings of lumbar motoneurons, focusing on the effects of apamin, a selective blocker of I_{KCa}. We measured the parameters of the sADP induced by a brief depolarization of the motoneurons. Application of apamin significantly increased the amplitude, duration, and area of the sADP, indicating a stronger and more prolonged depolarizing response when I_{KCa} is reduced (Fig. 4A-D). In addition, apamin also enhanced the capacity of motoneurons for bistable behavior. Specifically, motoneurons were able to express plateau potentials from more hyperpolarized holding potentials (Fig. 4E-F), reflected by a significant shift in Vh min from -62.6 mV to -64.8 mV ($p < 0.05$; Wilcoxon matched pairs test), and by increases in both the voltage range (ΔV) and the current range (ΔI) over which bistability was observed (Fig. 4G-H). Together, these results support the prediction of the model that reducing I_{KCa} expands the bistable regime by reducing the after-hyperpolarizing influence opposing I_{CAN}-driven depolarization (Figs. 1 and 3). These results underscore the antagonistic interplay between I_{CAN} and I_{KCa} in shaping motoneuron excitability and provide a mechanistic basis for bistable behaviors.

Modulation of I_{CAN}-based bistability by extracellular potassium concentration

Because I_{KCa} depends on the K^+ driving force, I_{CAN}-dependent bistability should be sensitive to the potassium reversal potential (E_K), which is set by the Nernst equation. This equation provides the potassium ion equilibrium potential based on the ratio of intracellular $[K^+]_i$ to extracellular $[K^+]_o$ potassium concentration (see Methods). Increasing extracellular potassium $[K^+]_o$ depolarizes E_K thereby reducing the outward driving force through I_{KCa}. This weakens the

hyperpolarizing influence of I_{KCa} that counteracts the I_{CAN}-mediated depolarizing feedback (see above).

We explored this interaction by varying $[K^+]_o$ and g_{CAN} in the model while holding g_{KCa} at 0.5 mS/cm^2. The resulting two-parameter map (Fig. 5B) shows the bistable range (color-coded width $\Delta I = I_{up} - I_{down}$, black indicating no bistability) as a function of g_{CAN} and $[K^+]_o$. At low $[K^+]_o$ (e.g., physiologically normal levels of 4 mM), E_K is strongly negative and I_{KCa} efficiently counteracts I_{CAN}, so relatively large g_{CAN} (e.g., ~1 mS/cm^2, Fig. 3A) is required for bistability. As $[K^+]_o$ increases, E_K depolarizes, weakening I_{KCa} and the bistable interval opens at progressively lower g_{CAN} (Fig. 5A). For instance, at g_{CAN} = 0.9 mS/cm^2 the model is not bistable at $[K^+]_o$ = 4 mM (Fig. 5C), but becomes bistable at $[K^+]_o$ = 8 mM (Figs. 5D, E), with the hysteresis width further expanding as $[K^+]_o$ rises (Fig. 5B). As elsewhere, we corroborated hysteresis with a step protocol showing different coexisting stable regimes at identical inputs (Fig. 5F).

This modulation is physiologically relevant: during sustained activity or in certain pathological conditions, elevation of $[K^+]_o$ can occur, which, by decreasing the effectiveness of I_{KCa}, would favour expression of the I_{CAN}-driven positive feedback and broaden the bistable operating range. More generally, these findings illustrate how intrinsic mechanisms of excitability can be tuned by extracellular milieu, here via the dependence of E_K on $[K^+]_o$.

The role of I_{NaP} in modulating I_{CAN}-based bistability

The persistent sodium current (I_{NaP}) is well-known for amplifying neuronal excitability by providing a sustained depolarizing drive at subthreshold voltages. To explore its influence on motoneuron bistability, we examined its interactions with I_{CAN} using our computational model (Fig. 6). The two-parameter bifurcation map in Fig. 6B depicts the bistability range (color-coded as the hysteresis width $\Delta I = I_{up} - I_{down}$) as a function of g_{NaP} and g_{CAN}. Overall, the bistable interval expands with increasing g_{NaP}, indicating that I_{NaP} enhances the robustness of bistability. For instance, at moderately low g_{CAN} values (e.g., 0.9 mS/cm^2; Fig. 6B), where I_{CAN} alone fails to produce bistability (Fig. 6C), elevating g_{NaP} from zero to 0.45 mS/cm^2 uncovers a clear hysteresis interval (Figs. 6B, D-F), enabling the coexistence of silent and spiking states over a range of injected currents.

This effect aligns with the core I_{CAN}-driven positive feedback loop underpinning bistability: (i) spiking activity opens voltage-gated calcium channels, leading to Ca^{2+} influx; (ii) this influx triggers CICR, amplifying the cytosolic Ca^{2+} signal; (iii) elevated $[Ca^{2+}]_i$ then activates I_{CAN}, and (iv) the resulting depolarisation accelerates spiking promoting additional Ca^{2+} entry and closing the self-reinforcing loop. Amplifying any element of this loop can elevate its overall gain, tipping the system toward bistability.

Here, I_{NaP} contributes by delivering a tonic depolarizing current that lowers the voltage threshold for spike initiation and Ca^{2+} entry. This facilitates the recruitment of I_{CAN} during the onset of activity and bolsters its ability to sustain the high-activity state once engaged, even at lower g_{CAN} levels. For example, at g_{CAN} = 0.9 mS/cm^2 and g_{NaP} = 0.45 mS/cm^2, the model displays robust bistability (Figs. 6D-F), whereas reducing g_{NaP} to 0 eliminates it (Fig. 6C). However, at lower I_{CAN}

expression (e.g., at g_{CAN} = 0.5 mS/cm^2), I_{NaP}-evoked depolarization is insufficient to achieve the high-gain regime needed for bistability at any g_{NaP}.

We tested these predictions pharmacologically in patch-clamp recorded lumbar motoneurons using veratridine, which at low micromolar concentrations enhances I_{NaP}. Following a short depolarizing pulse, veratridine increased the amplitude and area of the sADP, while shortening its duration (Fig. 7A-D), indicating a stronger depolarizing tail when I_{NaP} is enhanced. Veratridine also facilitated bistability: self-sustained spiking activity were triggered from more hyperpolarized holding potentials, with *Vh* shifting from -56.9 mV to -61.6 mV ($p < 0.01$; Wilcoxon matched pairs test). Both the voltage range (ΔV) and the current range (ΔI) supporting bistability increased (Fig. 7E-H).

Taken together, these findings support the model prediction that increasing I_{NaP} facilitates and broadens the operating window of I_{CAN}-driven bistability by enhancing depolarization while I_{CAN} remains the principal maintenance mechanism once engaged. This synergy between I_{CAN} and I_{NaP} helps explain how modest changes in persistent Na^+ conductance can markedly reshape motoneuron firing regimes.

Bistability based on I_{NaP} and the role of $[K^+]_o$

I_{NaP} could theoretically sustain bistability independently of I_{CAN} under conditions that maintain its activation between action potentials. For instance, if the inter-spike membrane potential remains above I_{NaP}'s deactivation threshold, I_{NaP} would provide a continuous depolarizing drive, creating a self-reinforcing loop where subthreshold depolarization promotes spiking, and the resulting activity further engages I_{NaP} without full reset. This mechanism might enable the neuron to toggle between quiescent and self-sustained firing states purely through sodium-based persistence, highlighting a potential alternative pathway for bistability in scenarios where calcium-dependent processes are minimized or absent.

In our model, when g_{CAN} = 0, I_{NaP} alone could not support bistability in the parameter range examined (Fig. 8A). The bifurcation diagram (Fig. 8D) elucidates this. At low injected current (I_{inj} < 0.85 μA/cm^2), the system's sole stable state is a low-voltage resting state (stable node). As I_{inj} surpasses this threshold, the node merges with a saddle point and subsequently ceases, leading to a stable limit cycle, which represents a spiking regime. A strong hyperpolarization follows each spike, dropping below the resting potential. This large post-spike hyperpolarization fully deactivates I_{NaP}, explaining its inability to maintain bistability independently. Consequently, when the injected current is decreased, the silent regime reappears via the same bifurcation, demonstrating an absence of hysteresis.

The post-spike hyperpolarization is mediated by K^+ outward currents and thus can be modulated by $[K^+]_o$, which sets the reversal potential E_K. Raising $[K^+]_o$ depolarizes E_K , thereby reducing the driving force of outward currents and diminishing the post-spike hyperpolarization. Under these conditions, I_{NaP} is less completely deactivated, allowing bistability to emerge (Figs. 8B, E).

As shown in Fig. 8E, when $[K^+]_o$ = 12 mM and I_{inj} crosses a value of 0.8 μA/cm^2, the resting state is lost through the same saddle-node bifurcation, but unlike at normal $[K^+]_o$, the trajectory joins a pre-existing spiking limit cycle with attenuated post-spike hyperpolarization (Figs. 8E, F). When I_{inj} is reduced, spiking persists down to 0.45 μA/cm^2, where the limit cycle intersects with the saddle point and disappears through a saddle-loop (homoclinic) bifurcation, and the system returns to resting state (Figs. 8E, F). Thus when I_{inj} falls between 0.45 and 0.85 μA/cm^2 both rest and spiking coexist, indicating a bistable regime (Fig. 8G). A distinctive feature of this type of bistability is that the resting potential lies below the voltage range of the limit cycle (spiking).

The presence and extent of bistable behavior depends jointly on g_{NaP} and $[K^+]_o$. At $[K^+]_o$ = 12 mM, bistability emerges once g_{NaP} exceeds ~0.2 mS/cm^2 (Fig. 8B), with the bistable interval widening as g_{NaP} increases. Mapping across parameters (Fig. 8C) shows that for g_{NaP} < 0.5 mS/cm^2 bistability requires $[K^+]_o$ > 10 mM; conversely, the bistability g_{NaP} threshold decreases as $[K^+]_o$ increases. For instance, with g_{NaP} = 0.25 mS/cm^2, bistability emerges once $[K^+]_o$ exceeds ~12 mM.

Together, these results indicate that while under normal conditions I_{NaP} alone is insufficient to produce bistability, elevated $[K^+]_o$ reduces outward current-mediated hyperpolarization, potentially enabling bistable firing.

The role of slowly inactivating potassium current ($I_{Kv1.2}$)

Recent work indicates that the potassium current mediated by Kv1.2 channels ($I_{Kv1.2}$) is prevalent in bistable motoneurons (Harris-Warrick et al., 2024), although its direct contribution to bistable behaviour has not been fully clarified. Kv1.2 channels inactivate very slowly during repetitive firing. In principle, such slow inactivation generates a positive feedback loop: as $I_{Kv1.2}$ gradually decreases during ongoing spiking, the cell becomes more excitable and can persist in an active state. On the other hand, when the neuron is silent, Kv1.2 channels are fully open and $I_{Kv1.2}$ can strongly oppose the initial depolarization.

To clarify $I_{Kv1.2}$ contribution, we simulated our computational model while varying both I_{inj} and $I_{Kv1.2}$'s maximal conductance, $g_{Kv1.2}$. In these simulations, $I_{Kv1.2}$ alone did not produce bistability between resting and spiking states. Instead, the model generated a regime of periodic bursting, alternating between spiking and quiescent phases, over an extremely narrow range of I_{inj}.

A signature of $I_{Kv1.2}$ is its effect on firing dynamics during constant depolarization: rather than stabilizing tonic firing, it induced a delayed excitation with ramping spike frequency (Bos et al., 2018). To isolate this effect, we removed both I_{CAN} and I_{NaP} (g_{NaP} = g_{CAN} = 0). Under these conditions (Fig. 9B), a rectangular current pulse elicited an initial fast depolarization followed by a slow secondary depolarization. If the stimulus was strong enough, this slow drift brought the neuron to a spiking threshold and then spiking began, with the firing rate progressively accelerating. This behavior reflects very slow inactivation kinetics of $I_{Kv1.2}$. Initially, $I_{Kv1.2}$ activates quickly, temporarily opposing depolarization, but then inactivates with a time constant of ~2.5 s

(see Methods), progressively reducing its own inhibitory effect and permitting further depolarization and firing.

By contrast, in absence of $I_{Kv1.2}$ but with I_{KCa} present, the model showed spike frequency adaptation (Fig. 9A). Here, firing decreased over time because I_{KCa} hyperpolarized the membrane. When both currents ($I_{Kv1.2}$ and I_{KCa}) were present, the firing dynamics (whether it shows ramping or adaptation) depended on their relative balance. This interaction can lead to complex dynamics where the slow inactivation of $I_{Kv1.2}$ competes with the calcium-dependent potassium currents tendency to stabilize or reduce firing frequency.

Discussion

In this study, we used a single-compartment computational model of spinal motoneurons to dissect the ionic mechanisms underlying bistability. Our results identify a minimal core mechanism based on the synergistic interactions among I_{CaL}, CICR, and I_{CAN} strongly modulated by I_{KCa}, I_{NaP} and $[K^+]_o$. These findings offer new insights into how bistable firing is generated and regulated in motoneurons.

Motoneuron bistability critically depends on the I_{CaL}-CICR-I_{CAN} loop

Early studies attributed plateau potentials and bistability to persistent L-type calcium currents (Schwindt & Crill, 1980; Hounsgaard, Hultborn, et al., 1988; Hounsgaard, Kiehn, et al., 1988; Hounsgaard & Mintz, 1988; Hounsgaard & Kiehn, 1989; Hounsgaard & Kjaerulff, 1992; Svirskis & Hounsgaard, 1997), a view reinforced by computational models requiring dendritic I_{CaL} to replicate these bistable behaviors (Booth & Rinzel, 1995; Booth et al., 1997; Carlin et al., 2000; ElBasiouny et al., 2005; Bui et al., 2006; Carlin et al., 2009; Kim & Jones, 2011). Immunohistochemical data further supported this interpretation by revealing the dendritic distribution of L-type Cav1.3 channels (Simon et al., 2003; Zhang et al., 2008). More recent findings have revealed a complementary mechanism, in which I_{CaL} primarily acts as a trigger, while other currents, notably the I_{CAN}, play a central role in mediating plateau potentials and bistability (Bos et al., 2021), as observed in motoneurons from neonatal and young adult murine models (Harris-Warrick et al., 2024).

Our computational findings reinforce and extend this view. The model shows that initial Ca^{2+} entry through I_{CaL} is insufficient to sustain bistability due to fast Ca^{2+} removal from the cytosol. The necessary amplification arises from CICR, linking I_{CaL}-mediated Ca^{2+} influx to intracellular stores. Accordingly, CICR surpasses the capacity of Ca^{2+} pumps to rapidly clear cytoplasmic Ca^{2+}, and therefore enables sustained intracellular Ca^{2+}, long-lasting I_{CAN} activation and bistability. Consistent with this, motoneuron bistability is abolished when CICR is inhibited, even though I_{CaL} currents are still present (Bouhadfane et al., 2013; Bos et al., 2021; Harris-Warrick et al., 2024). Together, I_{CaL}, CICR, and I_{CAN} emerge from the findings as a functional triad instrumental in motoneuron bistability. As such, the triad may provide a general feed-forward

mechanism for plateau generation across different structures of the CNS, owing to the fact that I_{CAN} also supports motor, sensory and memory-related plateaus (Fraser & MacVicar, 1996; Morisset & Nagy, 1999; Di Prisco et al., 2000; Yan et al., 2009; Toporikova & Butera, 2011; Jasinski et al., 2013).

Suppression of I_{CAN}-based bistability by I_{KCa}

The model adds a key regulatory layer to motoneuron bistability by clarifying the interplay between I_{CAN} and I_{KCa}. I_{KCa} dominance inhibits I_{CAN} -driven plateaus and prevents their formation. In line with the model, reducing I_{KCa} with apamin facilitates the expression of bistability and can unmask latent plateau potentials (Hounsgaard & Mintz, 1988; Hounsgaard & Kiehn, 1993).The relative contributions of I_{CAN} and I_{KCa} may tune the propensity to bistability across motoneuron subtypes. Bistability appears more frequently observed in large motoneurons (Harris-Warrick et al., 2024), a finding that, according to the assumption, would reflect a higher I_{CAN}/I_{KCa} ratio. This interpretation aligns with established physiological distinctions where large motoneurons, in line with size-dependent differential expression of SK channels (Deardorff et al., 2013), display brief AHPs, whereas small motoneurons exhibit prolonged AHPs (Kernell, 1965; Gustafsson & Pinter, 1984). In addition, large motoneurons generate stronger I_{CAN} than small motoneurons (Harris-Warrick et al., 2024).

Our model also identifies $[K^+]_o$ as a critical factor influencing I_{KCa} efficacy. Elevating $[K^+]_o$ depolarizes E_K, weakening I_{KCa} and shifting the balance towards I_{CAN}, thereby enhancing bistability (Fig. 4). Disruption of K^+ buffering through astrocytic Kir4.1 dysfunction in spinal cord injury (Olsen et al., 2010; Benson et al., 2023; Barbay et al., 2024), is likely to elevate $[K^+]_o$, paralleling findings from epilepsy studies (Djukic et al., 2007; Tong et al., 2014). A subsequent shift towards I_{CAN} is predicted to strengthen bistability and worsen spasticity (Bennett et al., 2001; C. Brocard et al., 2016).

Facilitation of I_{CAN}-mediated bistability by I_{NaP}

While I_{CAN} is the main driver of bistability, I_{NaP} acts as an essential modulator, extending the conditions under which bistability occurs. In our simulations, increasing I_{NaP} lowers the threshold for I_{CAN}-mediated bistability, enabling sustained firing even when I_{CAN} alone is insufficient (Fig. 6). Due to subthreshold depolarization (Crill, 1996) that enables repetitive spiking (Kuo et al., 2006), I_{NaP} biases the system towards I_{CaL}-CICR-I_{CAN} engagement and plateau generation. In line with this role, riluzole, an established inhibitor of I_{NaP}, reliably suppresses self-sustained firing in bistable motoneurons (Bouhadfane et al., 2013; Drouillas et al., 2023). At first glance, this might imply that plateau potentials depend directly on I_{NaP}. However, the persistence of TTX-resistant sADP after rizulole application (Bouhadfane et al., 2013; Drouillas et al., 2023) suggests that I_{CAN} provides the essential substrate for bistable behavior, while I_{NaP} serves as a facilitator. The I_{NaP} and I_{CAN} interaction extends beyond motoneurons; in the preBotzinger complex, for example, the two currents cooperate to produce rhythmic bursting (Jasinski et al., 2013; Phillips et al., 2019, 2022).

Under physiological conditions, I_{NaP} alone unlikely supports bistability because hyperpolarizing potassium currents deactivate I_{NaP} between spikes (Fig. 8). Elevating $[K^+]_o$ mitigates this hyperpolarization by depolarizing E_K, and allows I_{NaP} to create bistability at higher g_{NaP} (Fig. 8C). This has been clearly demonstrated in our simulations, where a pure I_{NaP}-based bistability emerges as $[K^+]_o$ approaches or exceeds 12 mM. This scenario may be relevant in SCI, where I_{NaP} is enhanced (Bennett et al., 2001; Li et al., 2004; Harvey et al., 2006; C. Brocard et al., 2016). In conjunction with high $[K^+]_o$, this enhancement can strengthen bistability and promote spasticity. Consequently, riluzole (Rilutek©), originally developed for ALS, is being explored to target spasticity in SCI patients (Cotinat et al., 2023).

The role of slowly inactivating potassium current ($I_{Kv1.2}$)

In spinal motoneurons, $I_{Kv1.2}$ imposes an initial brake on excitability and then relaxes over seconds, yielding delayed spiking and a characteristic ramping of discharge during sustained depolarization (Bos et al., 2018). Because this property scales with motoneuron size, larger α-motoneurons show stronger delayed excitation and ramping (Harris-Warrick et al., 2024). Yet, despite the greater prevalence of bistability in larger motoneurons, evidence for a generative role of Kv1.2 remains elusive. Our simulations clarify this point. Varying $I_{Kv1.2}$ in isolation never produced robust switching between silent and self-sustained firing states. Instead, it generated narrow-band bursting around a tight input window, while the hallmark hysteresis of bistability was absent. Mechanistically, $I_{Kv1.2}$ lacks the positive feedback needed to maintain a depolarized up-state. It is an outward conductance that weakens with use, modulating access to the plateau regime but not providing the sustaining inward drive. In contrast, stable bistability in both our model and experiments requires the I_{CaL}-CICR- I_{CAN} triad, a view reinforced by the identification of Trpm5 as the principal Na^+-permeable carrier of I_{CAN} underlying motoneuron plateaus (Bos et al., 2021). When TRPM5/I_{CAN} is suppressed, slow afterdepolarization and plateaus collapse even though $I_{Kv1.2}$ is intact, directly demonstrating that Kv1.2 is permissive rather than generative for bistability.

Serotonin and bistability

Brainstem-derived monoamines are central to motoneuron excitability and bistability (Heckman et al., 2008). In decerebrate cats, bistability depends on descending monoaminergic drive (Conway et al., 1988; Hounsgaard, Hultborn, et al., 1988; Lee & Heckman, 1998b, 1999). Acute spinalization removes these inputs and thereby reduces bistable properties of motoneurons, whereas monoamine reintroduction restores plateau potentials (Hounsgaard, Hultborn, et al., 1988). Among these modulators, serotonin is especially effective. In vertebrates, exogenous serotonin enhances excitability and bistability (Hounsgaard & Kiehn, 1985, 1989).

Mechanistically, serotonin acts primarily through 5-HT_2 receptors to amplify ionic currents that promote bistability. By increasing dendritic L-type calcium currents (Hounsgaard & Kiehn, 1989; Perrier & Hounsgaard, 2003; Perrier & Delgado-Lezama, 2005; Perrier & Cotel, 2008) it can promote calcium build-up and I_{CAN} activation as described in our model. Serotonin also shifts I_{NaP} activation toward hyperpolarized potentials, thereby amplifying neuronal excitability (Li & Bennett, 2003; Harvey et al., 2006). The shift enhances I_{NaP} and thus facilitates I_{CAN}-mediated

bistability. Finally, serotonin also reduces outward currents, notably I_{KCa}, thereby facilitating high-frequency firing (Grunnet et al., 2004). This serotonin-evoked reduction of I_{KCa} may lead to bistability in spinal motoneurons (Hounsgaard, Kiehn, et al., 1988; Hounsgaard & Kiehn, 1993), as demonstrated in our present modeling and experimental results.

The role of serotonin becomes especially evident during SCI, not because of its direct action, but rather because of its sudden loss following disruption of descending inputs. Initial serotonin depletion produces motoneurons hypofunction, otherwise known as “spinal shock” (Schadt & Barnes, 1980), mirroring the loss of bistability in our model upon blockade of I_{CAN} or CICR. However, with time, excitability and plateau potentials re-emerge, representing an electrophysiological correlate of chronic spasticity and hyperreflexia (Bennett et al., 2001). The rebound is attributed to plasticity in serotonin receptor signaling. Most notably, 5-HT_{2B} and 5-HT_{2C} receptors become constitutively active which restores persistent inward currents (e.g., I_{NaP}) and plateau firing even without serotonergic input (Li & Bennett, 2003; Murray et al., 2010, 2011; D’Amico et al., 2013; Tysseling et al., 2017). Consistent with this, our model shows that increased I_{NaP} strengthens I_{CAN}-driven bistability.

Limitations and future research directions

Dendritic calcium currents have been repeatedly linked to motoneuron plateaus and bistability (Booth et al., 1997; Carlin et al., 2000; Simon et al., 2003; ElBasiouny et al., 2005; Bui et al., 2006; Zhang et al., 2008). Our single-compartment computational model reproduces key features of motoneuron bistability, yet its simplified architecture cannot capture the full spatial complexity of motoneurons. By collapsing dendrites into a one compartment, our results indicate that a single-compartment approximation can support bistability (Booth et al., 1997; Carlin et al., 2000; ElBasiouny et al., 2005; Bui et al., 2006). They do not, however, exclude the possible specific role of dendrites. Indeed, dendritic I_{CaL} might amplify calcium signaling and could shape the expression and robustness of plateaus.

Our future work will include the construction and use of multi-compartment models to explore the role of spatial distribution of I_{CaL}, CICR, and I_{CAN} for testing how dendrite- versus soma-localized mechanisms affect bistability. In this context, establishing the precise subcellular localization of I_{CAN} channels remains a priority but progress is limited by the lack of highly specific antibodies to TRPM5, the presumed molecular correlate of I_{CAN} (Bos et al., 2021). Our analysis centers at L-type calcium channels only, but motoneurons also express T-type and N-type calcium channels (Umemiya & Berger, 1995; Hivert et al., 1995; Viana et al., 1997). Since these currents can complement or replace L-type currents in generating plateaus (Bouhadfane et al., 2013), future models may be instrumental in evaluating their contributions.

In summary, our minimal model captures the core features of bistable firing, with the ICaL-CICR-ICAN triad emerging as a central mechanism, while leaving open the contribution of dendritic processes. Future anatomically detailed models and experiments will be needed to resolve the effects of channels’ spatial distributions across motoneuron compartments.

Acknowledgements

This work was supported by the ANR MotoBis grant (ANR-24-CE16-1548-01) to F.B. and the NIH/NINDS grant (R01 NS130799) to I.A.R.

References

Barbay, T., Pecchi, E., Franco, J. J. R., Ivanov, A., Brocard, F., Rouach, N., & Bos, R. (2024). *Functional contribution of astrocytic Kir4.1 channels to spasticity after spinal cord injury*. Neuroscience. https://doi.org/10.1101/2024.10.11.617793

Bennett, D. J., Li, Y., & Siu, M. (2001). Plateau Potentials in Sacrocaudal Motoneurons of Chronic Spinal Rats, Recorded In Vitro. *Journal of Neurophysiology*, *86*(4), 1955–1971. https://doi.org/10.1152/jn.2001.86.4.1955

Benson, C. A., King, J. F., Kauer, S. D., Waxman, S. G., & Tan, A. M. (2023). Increased astrocytic GLT-1 expression in tripartite synapses is associated with SCI-induced hyperreflexia. *Journal of Neurophysiology*, *130*(5), 1358–1366. https://doi.org/10.1152/jn.00234.2023

Binder, M. D., Powers, R. K., & Heckman, C. J. (2020). Nonlinear Input-Output Functions of Motoneurons. *Physiology (Bethesda, Md.)*, *35*(1), 31–39. https://doi.org/10.1152/physiol.00026.2019

Boost C++ libraries (Version 1.86). (ver. 1.86). [C++]. https://www.boost.org/

Booth, V., & Rinzel, J. (1995). A minimal, compartmental model for a dendritic origin of bistability of motoneuron firing patterns. *Journal of Computational Neuroscience*, *2*(4), 299–312. https://doi.org/10.1007/BF00961442

Booth, V., Rinzel, J., & Kiehn, O. (1997). Compartmental Model of Vertebrate Motoneurons for Ca^{2+} -Dependent Spiking and Plateau Potentials Under Pharmacological Treatment. *Journal of Neurophysiology*, *78*(6), 3371–3385. https://doi.org/10.1152/jn.1997.78.6.3371

Bos, R., Drouillas, B., Bouhadfane, M., Pecchi, E., Trouplin, V., Korogod, S. M., & Brocard, F.

(2021). Trpm5 channels encode bistability of spinal motoneurons and ensure motor control of hindlimbs in mice. *Nature Communications*, *12*(1), 6815. https://doi.org/10.1038/s41467-021-27113-x

Bos, R., Harris-Warrick, R. M., Brocard, C., Demianenko, L. E., Manuel, M., Zytnicki, D., Korogod, S. M., & Brocard, F. (2018). Kv1.2 Channels Promote Nonlinear Spiking Motoneurons for Powering Up Locomotion. *Cell Reports*, *22*(12), 3315–3327. https://doi.org/10.1016/j.celrep.2018.02.093

Bouhadfane, M., Tazerart, S., Moqrich, A., Vinay, L., & Brocard, F. (2013). Sodium-Mediated Plateau Potentials in Lumbar Motoneurons of Neonatal Rats. *The Journal of Neuroscience*, *33*(39), 15626–15641. https://doi.org/10.1523/JNEUROSCI.1483-13.2013

Brocard, C., Plantier, V., Boulenguez, P., Liabeuf, S., Bouhadfane, M., Viallat-Lieutaud, A., Vinay, L., & Brocard, F. (2016). Cleavage of Na+ channels by calpain increases persistent Na+ current and promotes spasticity after spinal cord injury. *Nature Medicine*, *22*(4), 404–411. https://doi.org/10.1038/nm.4061

Brocard, F., Shevtsova, N. A., Bouhadfane, M., Tazerart, S., Heinemann, U., Rybak, I. A., & Vinay, L. (2013). Activity-dependent changes in extracellular Ca2+ and K+ reveal pacemakers in the spinal locomotor-related network. *Neuron*, *77*(6), 1047–1054. https://doi.org/10.1016/j.neuron.2013.01.026

Bui, T. V., Ter-Mikaelian, M., Bedrossian, D., & Rose, P. K. (2006). Computational estimation of the distribution of L-type Ca(2+) channels in motoneurons based on variable threshold of activation of persistent inward currents. *Journal of Neurophysiology*, *95*(1), 225–241. https://doi.org/10.1152/jn.00646.2005

Carlin, K. P., Bui, T. V., Dai, Y., & Brownstone, R. M. (2009). Staircase currents in motoneurons: Insight into the spatial arrangement of calcium channels in the dendritic tree. *The Journal of Neuroscience: The Official Journal of the Society for Neuroscience*, *29*(16), 5343–5353. https://doi.org/10.1523/JNEUROSCI.5458-08.2009

Carlin, K. P., Jones, K. E., Jiang, Z., Jordan, L. M., & Brownstone, R. M. (2000). Dendritic L-type calcium currents in mouse spinal motoneurons: Implications for bistability. *The European Journal of Neuroscience*, *12*(5), 1635–1646. https://doi.org/10.1046/j.1460-9568.2000.00055.x

Collins, D. F., Burke, D., & Gandevia, S. C. (2001). Large involuntary forces consistent with plateau-like behavior of human motoneurons. *The Journal of Neuroscience: The Official Journal of the Society for Neuroscience*, *21*(11), 4059–4065. https://doi.org/10.1523/JNEUROSCI.21-11-04059.2001

Conway, B. A., Hultborn, H., Kiehn, O., & Mintz, I. (1988). Plateau potentials in alpha-motoneurones induced by intravenous injection of L-dopa and clonidine in the spinal cat. *The Journal of Physiology*, *405*, 369–384. https://doi.org/10.1113/jphysiol.1988.sp017337

Cotinat, M., Boquet, I., Ursino, M., Brocard, C., Jouve, E., Alberti, C., Bensoussan, L., Viton, J.-M., Brocard, F., & Blin, O. (2023). Riluzole for treating spasticity in patients with chronic traumatic spinal cord injury: Study protocol in the phase ib/iib adaptive multicenter randomized controlled RILUSCI trial. *PloS One*, *18*(1), e0276892. https://doi.org/10.1371/journal.pone.0276892

Crill, W. E. (1996). Persistent sodium current in mammalian central neurons. *Annual Review of Physiology*, *58*, 349–362. https://doi.org/10.1146/annurev.ph.58.030196.002025

D'Amico, J. M., Murray, K. C., Li, Y., Chan, K. M., Finlay, M. G., Bennett, D. J., & Gorassini, M. A. (2013). Constitutively active 5-HT2/α1 receptors facilitate muscle spasms after human spinal cord injury. *Journal of Neurophysiology*, *109*(6), 1473–1484. https://doi.org/10.1152/jn.00821.2012

Deardorff, A. S., Romer, S. H., Deng, Z., Bullinger, K. L., Nardelli, P., Cope, T. C., & Fyffe, R. E. W. (2013). Expression of postsynaptic Ca2+-activated K+ (SK) channels at C-bouton synapses in mammalian lumbar -motoneurons. *The Journal of Physiology*, *591*(4),

875–897. https://doi.org/10.1113/jphysiol.2012.240879

Di Prisco, G. V., Pearlstein, E., Le Ray, D., Robitaille, R., & Dubuc, R. (2000). A cellular mechanism for the transformation of a sensory input into a motor command. *The Journal of Neuroscience: The Official Journal of the Society for Neuroscience*, *20*(21), 8169–8176. https://doi.org/10.1523/JNEUROSCI.20-21-08169.2000

Djukic, B., Casper, K. B., Philpot, B. D., Chin, L.-S., & McCarthy, K. D. (2007). Conditional knock-out of Kir4.1 leads to glial membrane depolarization, inhibition of potassium and glutamate uptake, and enhanced short-term synaptic potentiation. *The Journal of Neuroscience: The Official Journal of the Society for Neuroscience*, *27*(42), 11354–11365. https://doi.org/10.1523/JNEUROSCI.0723-07.2007

Drouillas, B., Brocard, C., Zanella, S., Bos, R., & Brocard, F. (2023). Persistent Nav1.1 and Nav1.6 currents drive spinal locomotor functions through nonlinear dynamics. *Cell Reports*, *42*(9), 113085. https://doi.org/10.1016/j.celrep.2023.113085

Eken, T., Hultborn, H., & Kiehn, O. (1989). Possible functions of transmitter-controlled plateau potentials in alpha motoneurones. *Progress in Brain Research*, *80*, 257–267; discussion 239-242. https://doi.org/10.1016/s0079-6123(08)62219-0

Eken, T., & Kiehn, O. (1989). Bistable firing properties of soleus motor units in unrestrained rats. *Acta Physiologica Scandinavica*, *136*(3), 383–394. https://doi.org/10.1111/j.1748-1716.1989.tb08679.x

ElBasiouny, S. M., Bennett, D. J., & Mushahwar, V. K. (2005). Simulation of Dendritic Ca_V 1.3 Channels in Cat Lumbar Motoneurons: Spatial Distribution. *Journal of Neurophysiology*, *94*(6), 3961–3974. https://doi.org/10.1152/jn.00391.2005

Fraser, D. D., & MacVicar, B. A. (1996). Cholinergic-Dependent Plateau Potential in Hippocampal CA1 Pyramidal Neurons. *The Journal of Neuroscience*, *16*(13), 4113–4128. https://doi.org/10.1523/JNEUROSCI.16-13-04113.1996

Gorassini, M. A., Bennett, D. J., & Yang, J. F. (1998). Self-sustained firing of human motor units.

Neuroscience Letters, *247*(1), 13–16. https://doi.org/10.1016/s0304-3940(98)00277-8

Gorassini, M., Bennett, D. J., Kiehn, O., Eken, T., & Hultborn, H. (1999). Activation patterns of hindlimb motor units in the awake rat and their relation to motoneuron intrinsic properties. *Journal of Neurophysiology*, *82*(2), 709–717. https://doi.org/10.1152/jn.1999.82.2.709

Grunnet, M., Jespersen, T., & Perrier, J.-F. (2004). 5-HT1A receptors modulate small-conductance Ca2+-activated K+ channels. *Journal of Neuroscience Research*, *78*(6), 845–854. https://doi.org/10.1002/jnr.20318

Gustafsson, B., & Pinter, M. J. (1984). Relations among passive electrical properties of lumbar alpha‐motoneurones of the cat. *The Journal of Physiology*, *356*(1), 401–431. https://doi.org/10.1113/jphysiol.1984.sp015473

Harris-Warrick, R. M., Pecchi, E., Drouillas, B., Brocard, F., & Bos, R. (2024). Effect of size on expression of bistability in mouse spinal motoneurons. *Journal of Neurophysiology*, *131*(4), 577–588. https://doi.org/10.1152/jn.00320.2023

Harvey, P. J., Li, Y., Li, X., & Bennett, D. J. (2006). Persistent sodium currents and repetitive firing in motoneurons of the sacrocaudal spinal cord of adult rats. *Journal of Neurophysiology*, *96 3*, 1141–1157.

Heckman, C. J., Johnson, M., Mottram, C., & Schuster, J. (2008). Persistent inward currents in spinal motoneurons and their influence on human motoneuron firing patterns. *The Neuroscientist: A Review Journal Bringing Neurobiology, Neurology and Psychiatry*, *14*(3), 264–275. https://doi.org/10.1177/1073858408314986

Heckman, C. J., Mottram, C., Quinlan, K., Theiss, R., & Schuster, J. (2009). Motoneuron excitability: The importance of neuromodulatory inputs. *Clinical Neurophysiology*, *120*(12), 2040–2054. https://doi.org/10.1016/j.clinph.2009.08.009

Hivert, B., Bouhanna, S., Diochot, S., Camu, W., Dayanithi, G., Henderson, C. E., & Valmier, J. (1995). Embryonic rat motoneurons express a functional P-type voltage-dependent

calcium channel. *International Journal of Developmental Neuroscience: The Official Journal of the International Society for Developmental Neuroscience*, *13*(5), 429–436. https://doi.org/10.1016/0736-5748(95)00026-d

Hounsgaard, J., Hultborn, H., Jespersen, B., & Kiehn, O. (1984). Intrinsic membrane properties causing a bistable behaviour of alpha-motoneurones. *Experimental Brain Research*, *55*(2), 391–394. https://doi.org/10.1007/BF00237290

Hounsgaard, J., Hultborn, H., Jespersen, B., & Kiehn, O. (1988). Bistability of alpha-motoneurones in the decerebrate cat and in the acute spinal cat after intravenous 5-hydroxytryptophan. *The Journal of Physiology*, *405*(1), 345–367. https://doi.org/10.1113/jphysiol.1988.sp017336

Hounsgaard, J., & Kiehn, O. (1985). Ca++ dependent bistability induced by serotonin in spinal motoneurons. *Experimental Brain Research*, *57*(2). https://doi.org/10.1007/BF00236551

Hounsgaard, J., & Kiehn, O. (1989). Serotonin-induced bistability of turtle motoneurones caused by a nifedipine-sensitive calcium plateau potential. *The Journal of Physiology*, *414*(1), 265–282. https://doi.org/10.1113/jphysiol.1989.sp017687

Hounsgaard, J., & Kiehn, O. (1993). Calcium spikes and calcium plateaux evoked by differential polarization in dendrites of turtle motoneurones in vitro. *The Journal of Physiology*, *468*, 245–259. https://doi.org/10.1113/jphysiol.1993.sp019769

Hounsgaard, J., Kiehn, O., & Mintz, I. (1988). Response properties of motoneurones in a slice preparation of the turtle spinal cord. *The Journal of Physiology*, *398*(1), 575–589. https://doi.org/10.1113/jphysiol.1988.sp017058

Hounsgaard, J., & Kjaerulff, O. (1992). Ca2+-Mediated Plateau Potentials in a Subpopulation of Interneurons in the Ventral Horn of the Turtle Spinal Cord. *The European Journal of Neuroscience*, *4*(2), 183–188. https://doi.org/10.1111/j.1460-9568.1992.tb00865.x

Hounsgaard, J., & Mintz, I. (1988). Calcium conductance and firing properties of spinal motoneurones in the turtle. *The Journal of Physiology*, *398*, 591–603.

https://doi.org/10.1113/jphysiol.1988.sp017059

Hultborn, H., Wigström, H., & Wängberg, B. (1975). Prolonged activation of soleus motoneurones following a conditioning train in soleus Ia afferents—A case for a reverberating loop? *Neuroscience Letters*, *1*(3), 147–152. https://doi.org/10.1016/0304-3940(75)90030-0

Jasinski, P. E., Molkov, Y. I., Shevtsova, N. A., Smith, J. C., & Rybak, I. A. (2013). Sodium and calcium mechanisms of rhythmic bursting in excitatory neural networks of the pre-Bötzinger complex: A computational modelling study. *European Journal of Neuroscience*, *37*(2), 212–230. https://doi.org/10.1111/ejn.12042

Jeter, R., & Molkov, Y. (2025). *Jeterlab/ionic-mechanisms-underlying-bistability-in-spinal-motoneurons* (Version pre-release) [Computer software]. Zenodo. https://doi.org/10.5281/zenodo.15527835

Kernell, D. (1965). The Limits of Firing Frequency in Cat Lumbosacral Motoneurones Possessing Different Time Course of Afterhyperpolarization. *Acta Physiologica Scandinavica*, *65*(1–2), 87–100. https://doi.org/10.1111/j.1748-1716.1965.tb04252.x

Kiehn, O., & Eken, T. (1997). Prolonged firing in motor units: Evidence of plateau potentials in human motoneurons? *Journal of Neurophysiology*, *78*(6), 3061–3068. https://doi.org/10.1152/jn.1997.78.6.3061

Kim, H., & Jones, K. E. (2011). Asymmetric electrotonic coupling between the soma and dendrites alters the bistable firing behaviour of reduced models. *Journal of Computational Neuroscience*, *30*(3), 659–674. https://doi.org/10.1007/s10827-010-0284-x

Kuo, J. J., Lee, R. H., Zhang, L., & Heckman, C. J. (2006). Essential role of the persistent sodium current in spike initiation during slowly rising inputs in mouse spinal neurones. *The Journal of Physiology*, *574*(3), 819–834. https://doi.org/10.1113/jphysiol.2006.107094

Lee, R. H., & Heckman, C. J. (1998a). Bistability in Spinal Motoneurons In Vivo: Systematic Variations in Persistent Inward Currents. *Journal of Neurophysiology*, *80*(2), 583–593. https://doi.org/10.1152/jn.1998.80.2.583

Lee, R. H., & Heckman, C. J. (1998b). Bistability in spinal motoneurons in vivo: Systematic variations in rhythmic firing patterns. *Journal of Neurophysiology*, *80*(2), 572–582. https://doi.org/10.1152/jn.1998.80.2.572

Lee, R. H., & Heckman, C. J. (1999). Enhancement of Bistability in Spinal Motoneurons In Vivo by the Noradrenergic α_1 Agonist Methoxamine. *Journal of Neurophysiology*, *81*(5), 2164–2174. https://doi.org/10.1152/jn.1999.81.5.2164

Li, Y., & Bennett, D. J. (2003). Persistent sodium and calcium currents cause plateau potentials in motoneurons of chronic spinal rats. *Journal of Neurophysiology*, *90*(2), 857–869. https://doi.org/10.1152/jn.00236.2003

Li, Y., Gorassini, M. A., & Bennett, D. J. (2004). Role of Persistent Sodium and Calcium Currents in Motoneuron Firing and Spasticity in Chronic Spinal Rats. *Journal of Neurophysiology*, *91*(2), 767–783. https://doi.org/10.1152/jn.00788.2003

Morisset, V., & Nagy, F. (1999). Ionic Basis for Plateau Potentials in Deep Dorsal Horn Neurons of the Rat Spinal Cord. *The Journal of Neuroscience*, *19*(17), 7309–7316. https://doi.org/10.1523/JNEUROSCI.19-17-07309.1999

Murray, K. C., Nakae, A., Stephens, M. J., Rank, M., D'Amico, J., Harvey, P. J., Li, X., Harris, R. L. W., Ballou, E. W., Anelli, R., Heckman, C. J., Mashimo, T., Vavrek, R., Sanelli, L., Gorassini, M. A., Bennett, D. J., & Fouad, K. (2010). Recovery of motoneuron and locomotor function after spinal cord injury depends on constitutive activity in 5-HT2C receptors. *Nature Medicine*, *16*(6), 694–700. https://doi.org/10.1038/nm.2160

Murray, K. C., Stephens, M. J., Ballou, E. W., Heckman, C. J., & Bennett, D. J. (2011). Motoneuron excitability and muscle spasms are regulated by 5-HT2B and 5-HT2C receptor activity. *Journal of Neurophysiology*, *105*(2), 731–748.

https://doi.org/10.1152/jn.00774.2010

Olsen, M. L., Campbell, S. C., McFerrin, M. B., Floyd, C. L., & Sontheimer, H. (2010). Spinal cord injury causes a wide-spread, persistent loss of Kir4.1 and glutamate transporter 1: Benefit of 17 beta-oestradiol treatment. *Brain: A Journal of Neurology*, *133*(Pt 4), 1013–1025. https://doi.org/10.1093/brain/awq049

Perrier, J.-F., & Cotel, F. (2008). Serotonin differentially modulates the intrinsic properties of spinal motoneurons from the adult turtle. *The Journal of Physiology*, *586*(5), 1233–1238. https://doi.org/10.1113/jphysiol.2007.145706

Perrier, J.-F., & Delgado-Lezama, R. (2005). Synaptic release of serotonin induced by stimulation of the raphe nucleus promotes plateau potentials in spinal motoneurons of the adult turtle. *The Journal of Neuroscience: The Official Journal of the Society for Neuroscience*, *25*(35), 7993–7999. https://doi.org/10.1523/JNEUROSCI.1957-05.2005

Perrier, J.-F., & Hounsgaard, J. (2003). 5-HT2 receptors promote plateau potentials in turtle spinal motoneurons by facilitating an L-type calcium current. *Journal of Neurophysiology*, *89*(2), 954–959. https://doi.org/10.1152/jn.00753.2002

Phillips, R. S., John, T. T., Koizumi, H., Molkov, Y. I., & Smith, J. C. (2019). Biophysical mechanisms in the mammalian respiratory oscillator re-examined with a new data-driven computational model. *Elife*, *8*, e41555.

Phillips, R. S., Koizumi, H., Molkov, Y. I., Rubin, J. E., & Smith, J. C. (2022). Predictions and experimental tests of a new biophysical model of the mammalian respiratory oscillator. *Elife*, *11*, e74762.

Schadt, J. C., & Barnes, C. D. (1980). Motoneuron membrane changes associated with spinal shock and the Schiff-Sherrington phenomenon. *Brain Research*, *201*(2), 373–383. https://doi.org/10.1016/0006-8993(80)91041-0

Schwindt, P. C., & Crill, W. E. (1980). Properties of a persistent inward current in normal and TEA-injected motoneurons. *Journal of Neurophysiology*, *43*(6), 1700–1724.

https://doi.org/10.1152/jn.1980.43.6.1700

Simon, M., Perrier, J.-F., & Hounsgaard, J. (2003). Subcellular distribution of L-type Ca2+ channels responsible for plateau potentials in motoneurons from the lumbar spinal cord of the turtle. *The European Journal of Neuroscience*, *18*(2), 258–266. https://doi.org/10.1046/j.1460-9568.2003.02783.x

Svirskis, G., & Hounsgaard, J. (1997). Depolarization-induced facilitation of a plateau-generating current in ventral horn neurons in the turtle spinal cord. *Journal of Neurophysiology*, *78*(3), 1740–1742. https://doi.org/10.1152/jn.1997.78.3.1740

Tong, X., Ao, Y., Faas, G. C., Nwaobi, S. E., Xu, J., Haustein, M. D., Anderson, M. A., Mody, I., Olsen, M. L., Sofroniew, M. V., & Khakh, B. S. (2014). Astrocyte Kir4.1 ion channel deficits contribute to neuronal dysfunction in Huntington's disease model mice. *Nature Neuroscience*, *17*(5), 694–703. https://doi.org/10.1038/nn.3691

Toporikova, N., & Butera, R. J. (2011). Two types of independent bursting mechanisms in inspiratory neurons: An integrative model. *Journal of Computational Neuroscience*, *30*(3), 515–528. https://doi.org/10.1007/s10827-010-0274-z

Tysseling, V. M., Klein, D. A., Imhoff-Manuel, R., Manuel, M., Heckman, C. J., & Tresch, M. C. (2017). Constitutive activity of 5-HT2C receptors is present after incomplete spinal cord injury but is not modified after chronic SSRI or baclofen treatment. *Journal of Neurophysiology*, *118*(5), 2944–2952. https://doi.org/10.1152/jn.00190.2017

Umemiya, M., & Berger, A. J. (1995). Single-channel properties of four calcium channel types in rat motoneurons. *The Journal of Neuroscience: The Official Journal of the Society for Neuroscience*, *15*(3 Pt 2), 2218–2224. https://doi.org/10.1523/JNEUROSCI.15-03-02218.1995

Viana, F., Van den Bosch, L., Missiaen, L., Vandenberghe, W., Droogmans, G., Nilius, B., & Robberecht, W. (1997). Mibefradil (Ro 40-5967) blocks multiple types of voltage-gated calcium channels in cultured rat spinal motoneurones. *Cell Calcium*, *22*(4), 299–311.

https://doi.org/10.1016/s0143-4160(97)90068-3

Yan, H.-D., Villalobos, C., & Andrade, R. (2009). TRPC Channels Mediate a Muscarinic Receptor-Induced Afterdepolarization in Cerebral Cortex. *The Journal of Neuroscience*, *29*(32), 10038–10046. https://doi.org/10.1523/JNEUROSCI.1042-09.2009

Zhang, M., Møller, M., Broman, J., Sukiasyan, N., Wienecke, J., & Hultborn, H. (2008). Expression of calcium channel Ca_V 1.3 in cat spinal cord: Light and electron microscopic immunohistochemical study. *Journal of Comparative Neurology*, *507*(1), 1109–1127. https://doi.org/10.1002/cne.21595

Zhang, M., Sukiasyan, N., Møller, M., Bezprozvanny, I., Zhang, H., Wienecke, J., & Hultborn, H. (2006). Localization of L-type calcium channel Ca(V)1.3 in cat lumbar spinal cord—With emphasis on motoneurons. *Neuroscience Letters*, *407*(1), 42–47. https://doi.org/10.1016/j.neulet.2006.07.073

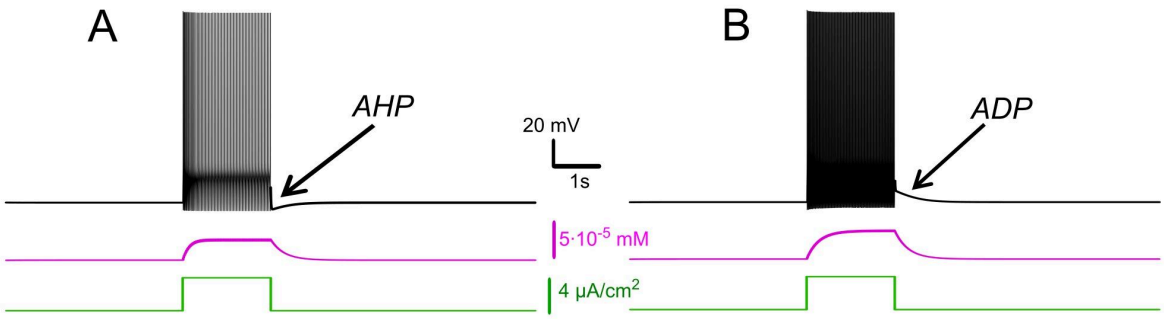

Figure 1. Effects of I_{KCa} vs. effects of I_{CAN}. Membrane potential (black) and intracellular Ca^{2+} (magenta) in response to step current (green). Intracellular Ca^{2+} concentration increases during spiking activity and then slowly adapts. **A**. When I_{KCa} is stronger than I_{CAN} (g_{KCa}=0.5 mS, g_{CAN}=0 mS), this leads to after-hyperpolarization (AHP). **B**. When I_{CAN} is stronger than I_{KCa} (g_{KCa}=0.5 mS, g_{CAN}=0.7 mS), this leads to after-depolarization (ADP) immediately following spiking activity.

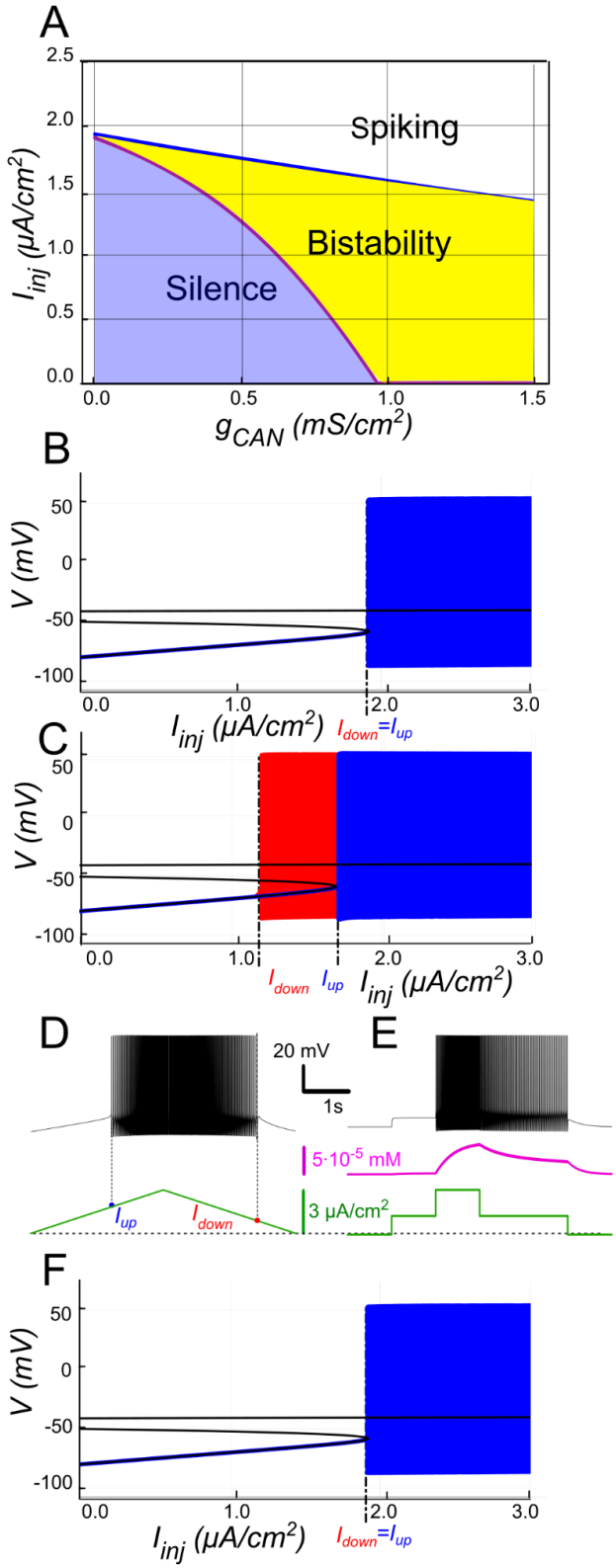

Figure 2. I_{CAN} -induced bistability and its disappearance after CIRC blockade. A: Parameter plane (g_{CAN}, I_{inj}) partitioned into regions of different behaviors. The upper and lower boundaries of the bistability region represent the dependence of I_{up} (blue line) and I_{down} (red line) on g_{CAN}, respectively. With no I_{CAN} (g_{CAN} = 0) the transitions from silence to spiking and back occur at the same I_{inj} values signifying no bistability. As g_{CAN} increases, I_{down} becomes smaller than I_{up}, with the bistability range progressively expanding. **B, C**: **Bifurcation diagrams showing different behaviors of the system** at g_{CAN} = 0 and g_{CAN} = 0.5 mS/cm^2 across a range of the injected current values, I_{inj}. Black line depicts the system's equilibrium states. When $I_{inj} < I_{up}$ there is a stable hyperpolarized state (stable node). If I_{inj} is increased over I_{up}, the system transitions to spiking, covering the voltage range shown in red and blue. This stable spiking regime exists in the range $I_{inj} > I_{down}$. When I_{inj} is reduced below I_{down}, the limit cycle representing spiking disappears, and the system transitions to the low voltage stable fixed point. Between these bifurcation points the hyperpolarized state (silence) coexists with the stable limit cycle (spiking) shown in red**. D, E: Bistability revealed with ramp and step protocols**. **D**: I_{inj} was linearly increased from 0 to 3 $\mu A/cm^2$ and back (green). Note that spiking started at higher current than the transition back to silence ($I_{up} > I_{down}$). **E**: I_{inj} was held piecewise constant at 0 first, then increased to 1.5 $\mu A/cm^2$, then to 3, then reduced back to 1.5, and, finally, to 0 (see the black trace at the bottom). At I_{inj} = 1.5 $\mu A/cm^2$ the system exhibits spiking or silence depending on whether it was active or not during the previous stage. Note the difference in the intracellular calcium concentration levels (green trace). **F**. Same representation as in C but with intracellular calcium release blocked (k_{CIRC} = 0). Note lack of bistability.

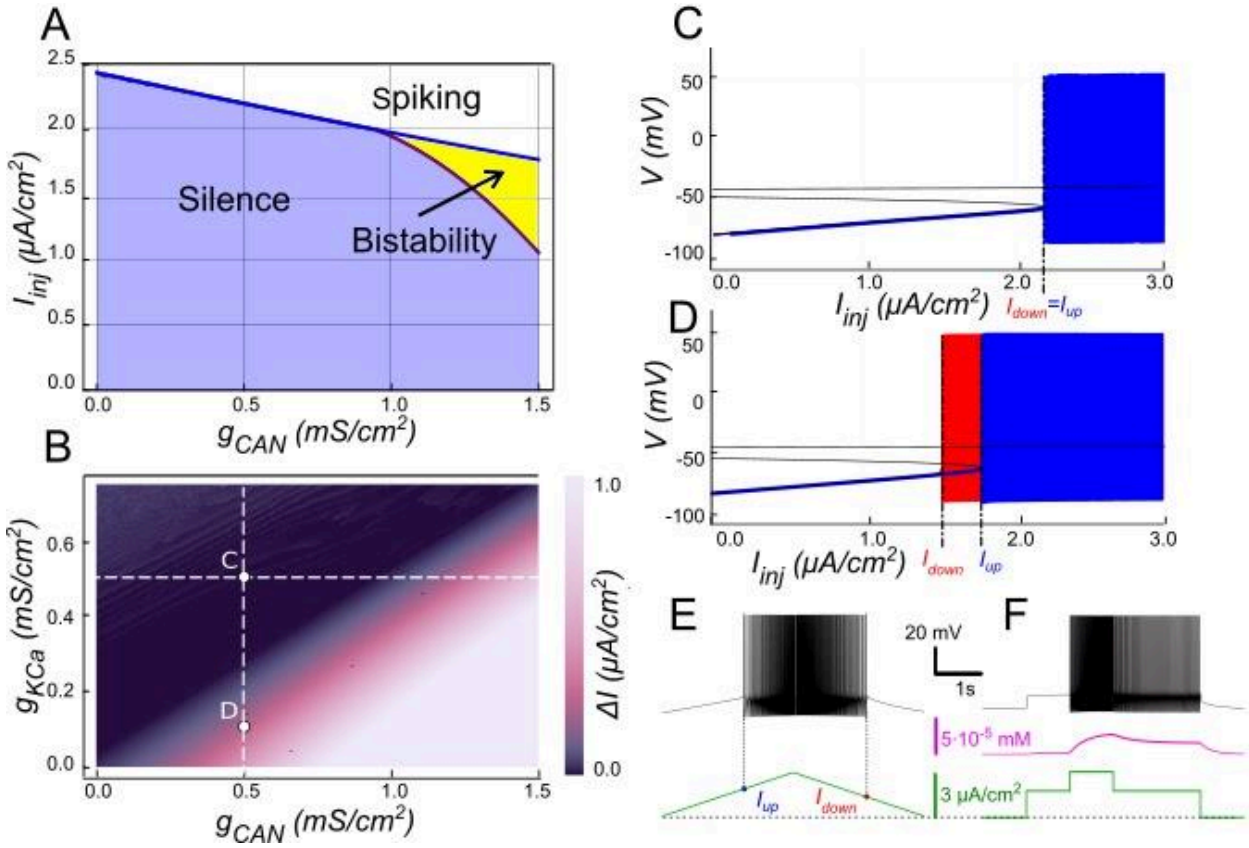

Figure 3. Modulation of I_{CAN}-dependent bistability by I_{KCa}. **A**. Bifurcation diagram similar to Fig. 2A, constructed for g_{KCa} = 0.5 *mS/cm²*. Note, that unlike in Fig. 2, bistability emerges once g_{CAN} exceeds 1 *mS/cm²*. **B**. Bistability range ΔI_{inj} depending on g_{CAN} and g_{KCa} conductances. Bistability range (defined as I_{up} - I_{down}) is color coded. Bistability exists in the lower right part of the diagram. Note near linear dependence of g_{CAN} bistability threshold on g_{KCa}. White dashed line shows the value of g_{KCa} used to construct the bifurcation diagram in panel A. **C, D**. Bifurcation diagrams showing possible behaviors of the system at the parameter values labelled correspondingly in panel B. **C**. At higher g_{KCa} value (g_{KCa} = 0.5) transitions from quiescence to spiking and back occur at the same injected current value (I_{up} = I_{down}), indicating no bistability. **D**. When g_{KCa} is lowered to 0.1, the transition from spiking to quiescence occurs at a lower injected current than the transition from quiescence to spiking (I_{down} < I_{up}), so spiking shown in red coexists with the silent regime. **E**. Ramp (left) and step (right) current injection protocols, illustrating bistability revealed in D. The intermediate current step is between I_{down} and I_{up}. The system's state depends on whether it was active or not at the previous step, exhibiting bistable behavior.

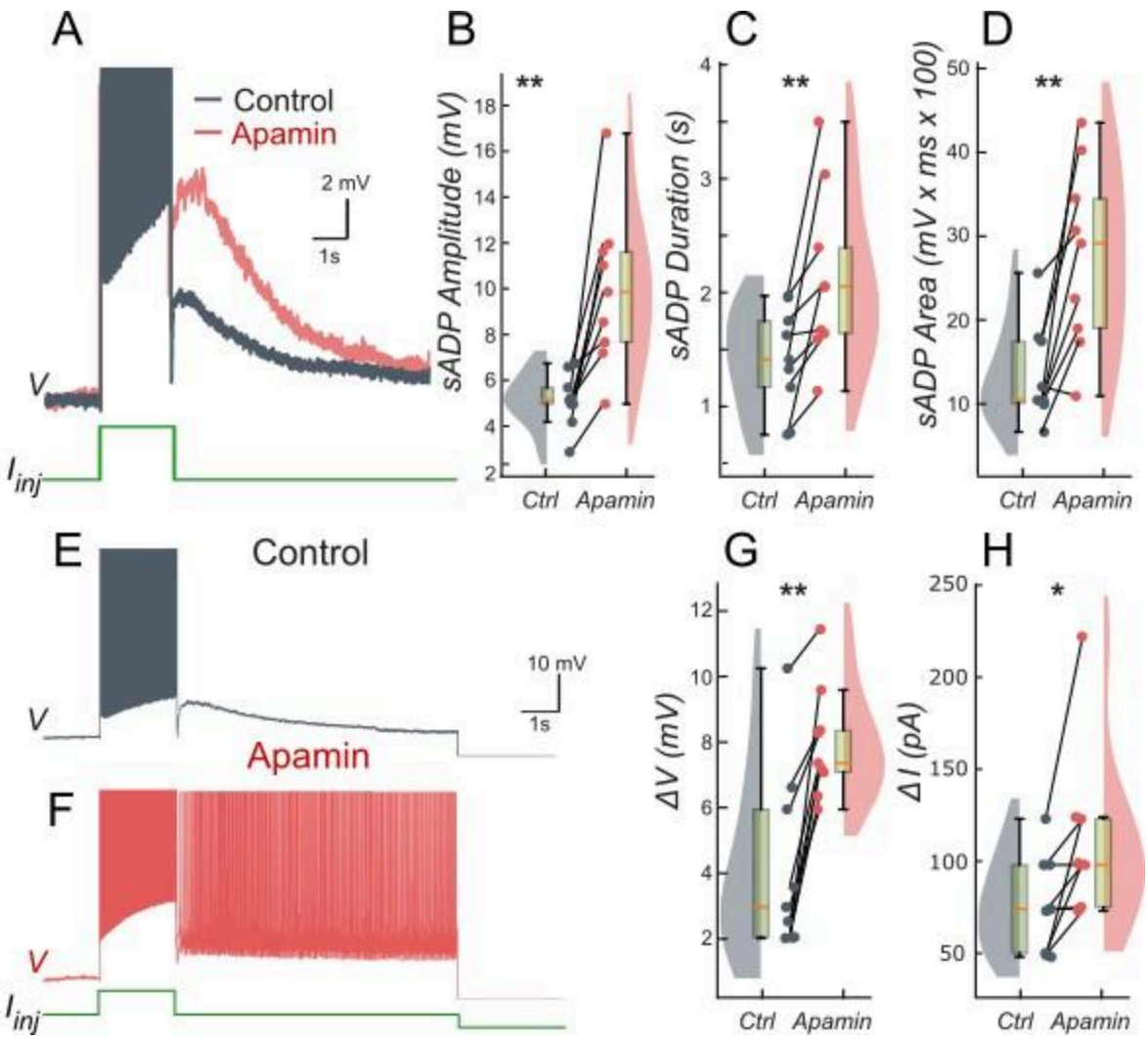

Figure 4. **Ca^{2+}-activated K+ current (I_{KCa}) limits the slow afterdepolarization and membrane bistability in lumbar motoneurons. A**: Superimposed voltage traces recorded in the same motoneuron during a brief (2 s) depolarizing current step (bottom) under control conditions (black) and after bath application of apamin (red). **B-D**: Quantification of the sADP amplitude (**B**), duration(**C**) and area (**D**). **E, F**: Voltage traces in response to a 2-s depolarizing pulse before (**E**) and after apamin (**F**). **G, H:** Quantification of bistability through ΔV and ΔI. ΔV and ΔI represent the range of holding potentials and holding currents, respectively, over which self-sustained firing can be observed. Each is defined as the difference between the most depolarized and the most hyperpolarized value (potential for ΔV, current for ΔI) at which self-sustained firing is triggered or maintained (see Methods). Paired data from individual motoneurons (n = 9) are linked and overlaid on violin and box-and-whisker plots. *P < 0.05, **P < 0.01, two-tailed Wilcoxon signed-rank test.

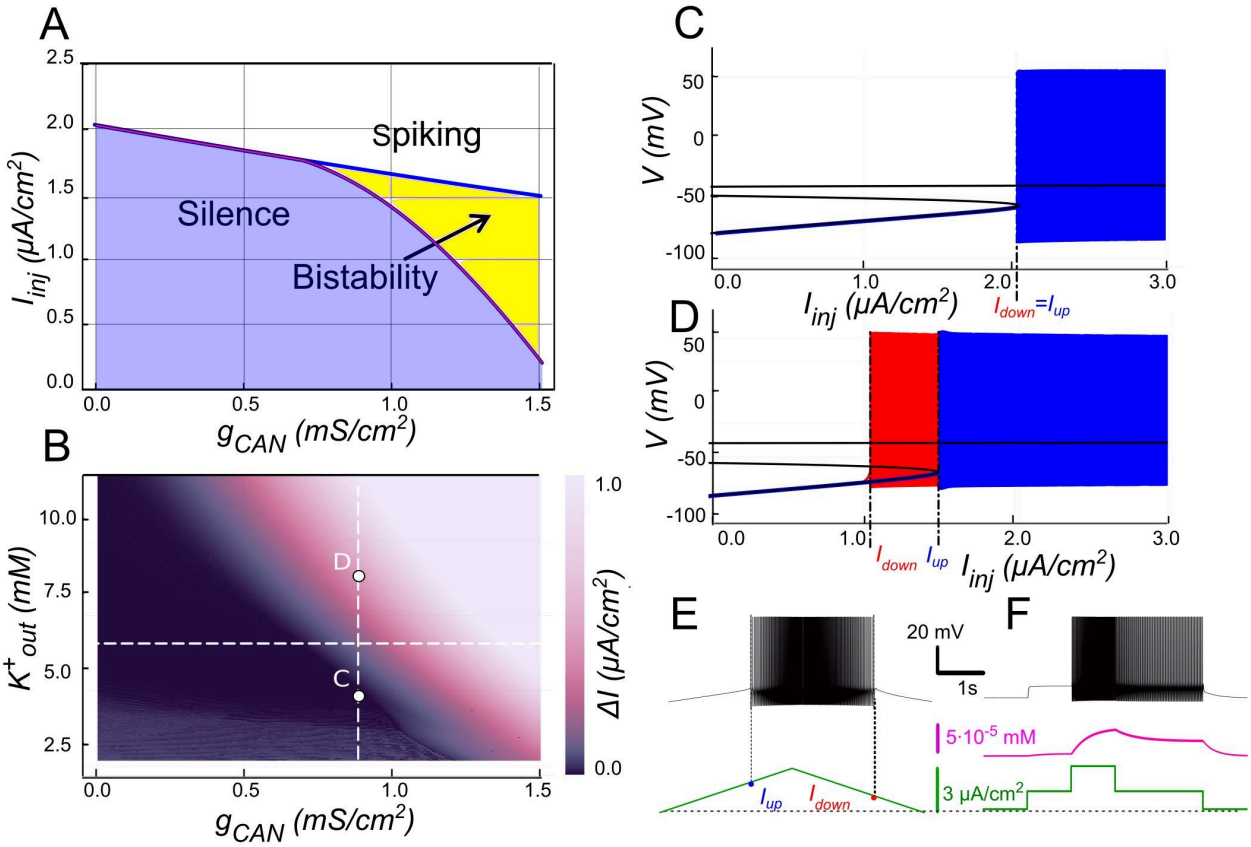

Figure 5. **Modulation of I_{CAN}-dependent bistability by extracellular potassium concentration ($[K^+]_o$)**. **A**. Bifurcation diagram similar to Fig. 3A, constructed for g_{KCa} = 0.5 *mS/cm*², but at elevated $[K^+]_o$ = 6mM instead of physiologically normal 4mM. Note, that compared to Fig. 3A, bistability emerges at lower g_{CAN}. **B**. Color-coded bistability range (I_{up} - I_{down}) depending on g_{CAN} and $[K^+]_o$. Black area corresponds to no bistability. White dashed line shows the $[K^+]_o$ value used in panel A. g_{CAN} bifurcation value reduces as $[K^+]_o$ increases, therefore an increase in $[K^+]_o$ can lead to bistability emergence, as shown in **C** and **D**. If g_{CAN} = 0.9 *mS/cm*², at $[K^+]_o$ = 4 mM (physiologically normal value) no bistability exists (**B**), but if $[K^+]_o$ is raised to 8 mM, bistability emerges (**C**), as illustrated by ramp (**E**) and step (**F**) current protocols.

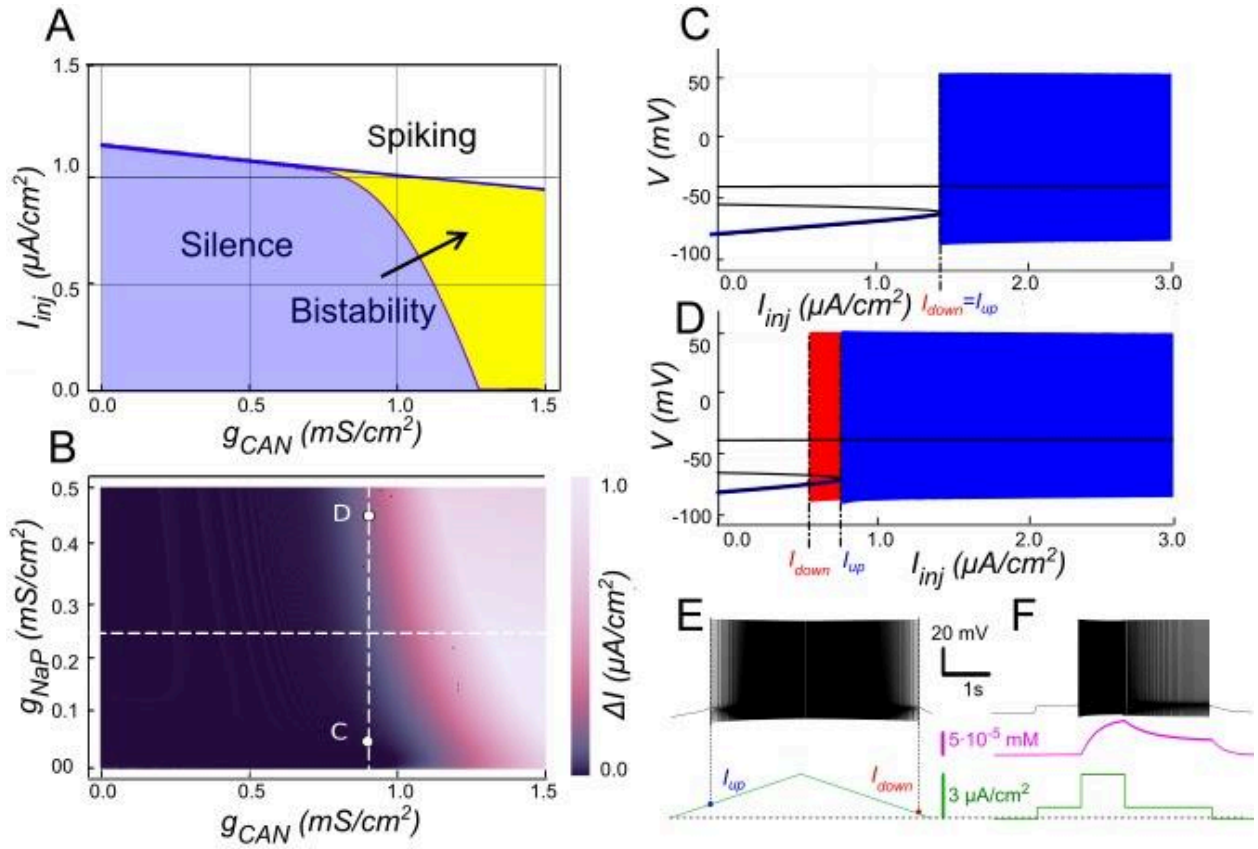

Figure 6. **Modulation of I_{CAN}-dependent bistability by I_{NaP}. A**. Bifurcation diagram similar to Fig. 3A, constructed for g_{KCa} = 0.5 *mS/cm²*, but at g_{NaP} = 0.25 *mS/cm²* instead of zero. Note, that compared to Fig. 3A, bistability emerges at lower g_{CAN}**. B**. Color-coded bistability range (I_{up} - I_{down}) depending on g_{CAN} and g_{NaP} with g_{KCa} fixed at 0.5 *mS/cm²*. Black area corresponds to no bistability. g_{CAN} bifurcation value reduces as g_{NaP} increases, therefore an increase in g_{NaP} can lead to bistability emergence, as shown in **C** and **D**. If g_{CAN} = 0.9 *mS/cm²*, at g_{NaP} = 0 no bistability exists (**C**), but if g_{NaP} is raised to 0.45 *mS/cm²*, bistability emerges (**D**), as illustrated by ramp (**E**) and step current protocols (**F**).

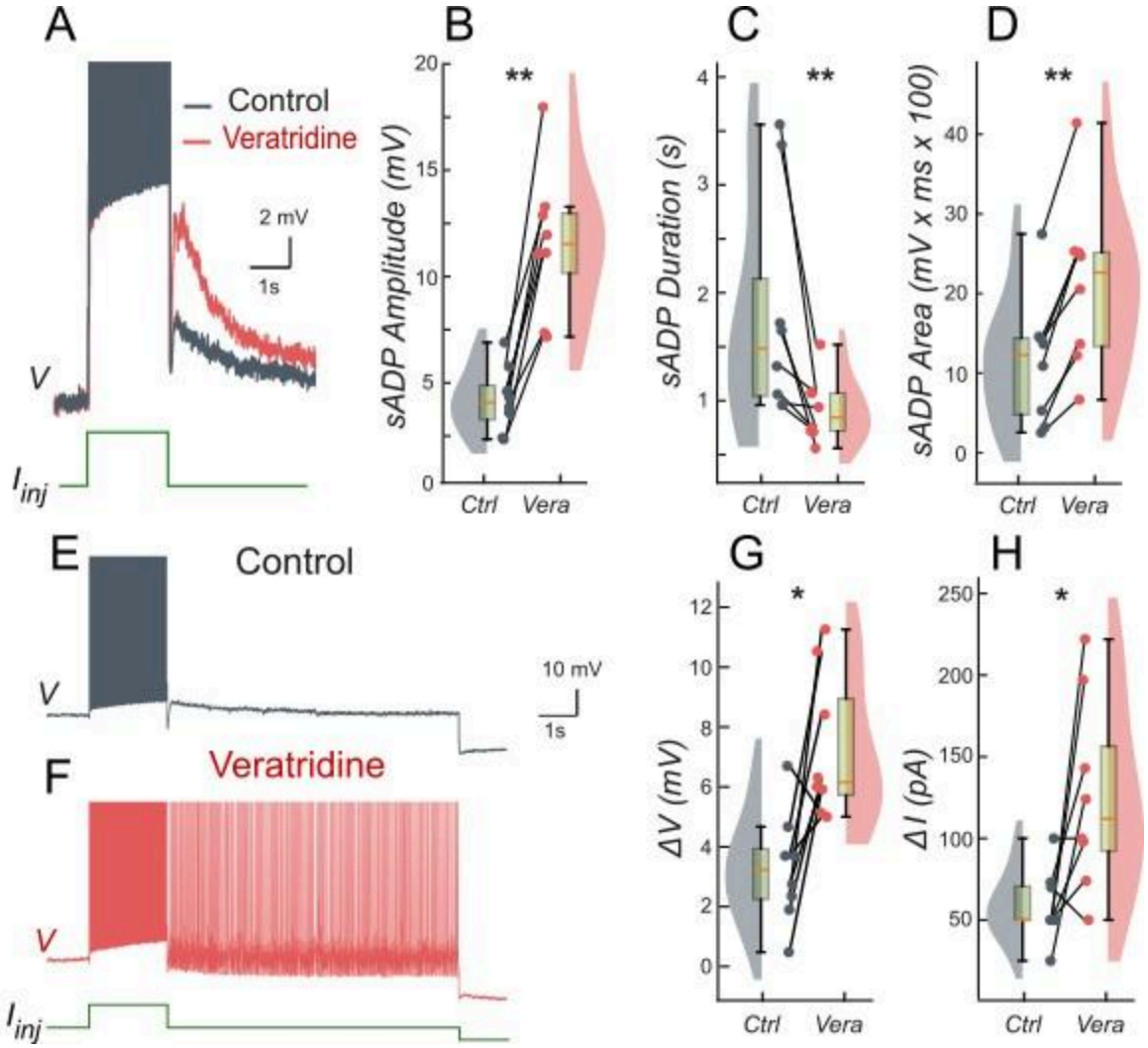

Figure 7. **Persistent Na^+ current (I_{NaP}) facilitates the slow afterdepolarization and membrane bistability in lumbar motoneurons. A**: Superimposed voltage traces recorded in the same motoneuron during a brief (2 s) depolarizing current step (bottom) under control conditions (black) and after bath application of veratridine (red). **B-D**: Quantification of the sADP amplitude (**B**), duration (**C**) and area (**D**). **E, F**: Voltage traces in response to a 2-s depolarizing pulse before (**E**) and after veratridine (**F**). **G, H:** Quantification of bistability through ΔV and ΔI. ΔV and ΔI represent the range of holding potentials and holding currents, respectively, over which self-sustained firing can be observed. Each is defined as the difference between the most depolarized and the most hyperpolarized value (potential for ΔV, current for ΔI) at which self-sustained firing is triggered or maintained (see Methods). Paired data from individual motoneurons (n = 8) are linked and overlaid on violin and box-and-whisker plots. *P < 0.05, **P < 0.01, two-tailed Wilcoxon signed-rank test.

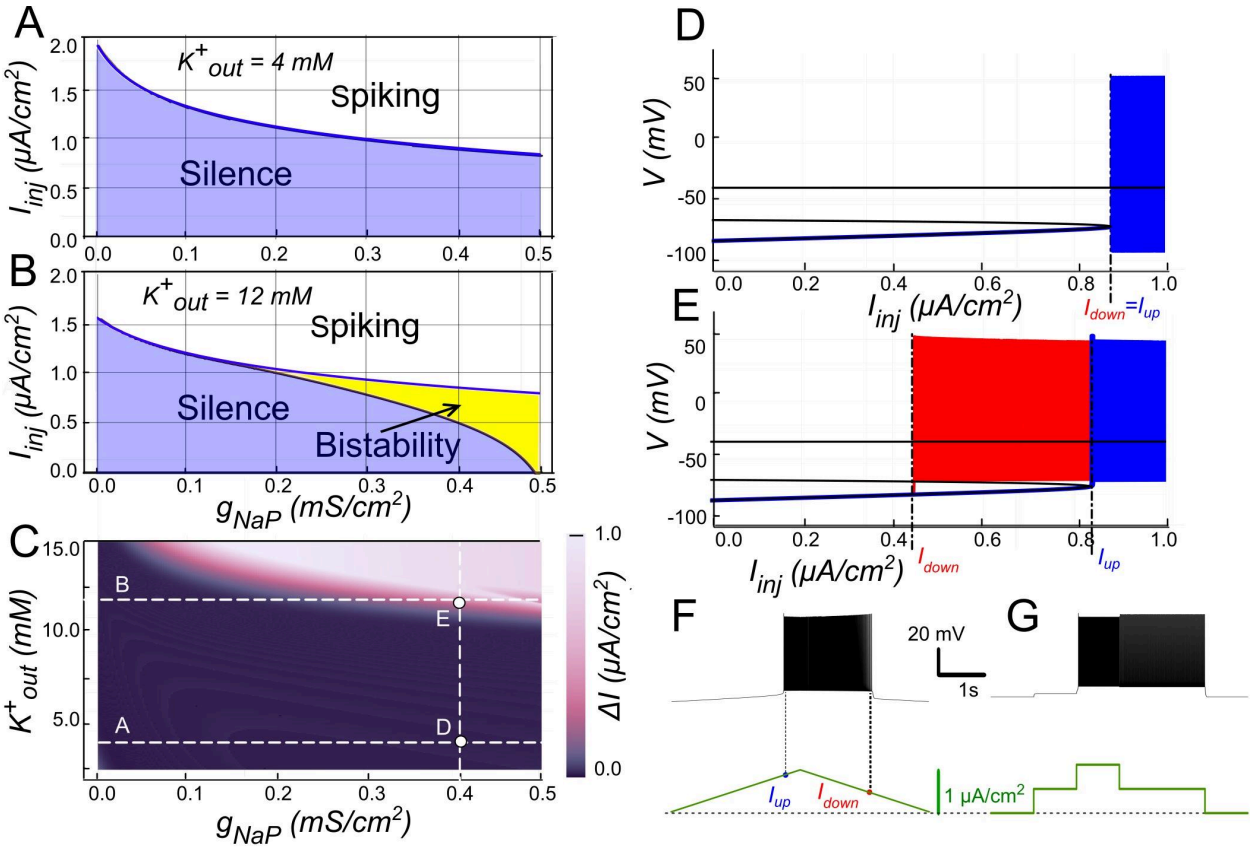

Figure 8. **Bistability based on I_{NaP} and the role of $[K^+]_o$**. **A**. Activity regimes of the model neuron depending on the injected current (I_{inj}) and the conductance of persistent sodium current (g_{NaP}) at baseline K^+ extracellular concentration ($[K^+]_o$ = 4mM). At all values of g_{NaP} as the injected current changes, the model transitions from silence to spiking and back with no hysteresis which indicates no bistability. **B**. Activity patterns of the model neuron depending on the injected current and g_{NaP} conductance at $[K^+]_o$ = 12 mM. Once g_{NaP} exceeds approximately 0.15 mS/cm^2, bistability emerges. **C**. Adjusting the sodium persistent inward current (I_{NaP}) conductance (g_{NaP}) and extracellular potassium concentration ($[K^+]_o$) in a model neuron reveals bistable regimes. The range of injected current where bistability occurs is shown in color, with black indicating no bistability. Higher $[K^+]_o$ levels require smaller g_{NaP} for bistability, suggesting that increased $[K^+]_o$ can induce bistability in neurons with otherwise insufficient g_{NaP} expression. **D**. at g_{NaP} = 0.4 mS/cm^2 and $[K^+]_o$ = 4 mM no bistability is observed. **E**. However, as $[K^+]_o$ is increased to 12 mM, bistability emerges, as illustrated by ramp (**F**) and step current protocols (**G**).

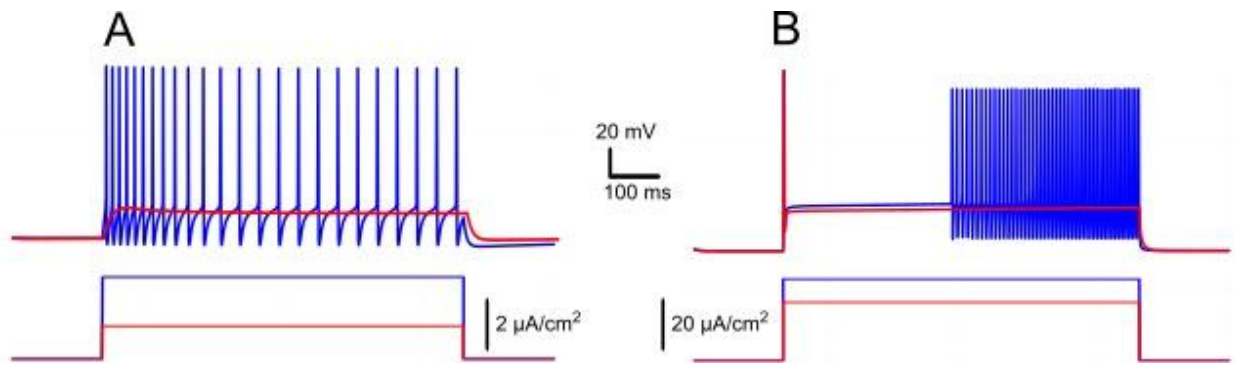

Figure 9. Ramp/delayed excitation versus spike frequency adaptation in response to rectangular current injection. A. Model response with I_{KCa} alone ($g_{Kv1.2}$ = 0, g_{KCa} = 1 *mS/cm²*, g_{NaP} = g_{CAN} = 0), displaying spike frequency adaptation as I_{KCa} activation hyperpolarizes the neuron, reducing firing rate over time. **B**. Model response with $I_{Kv1.2}$ alone ($g_{Kv1.2}$ = 2 *mS/cm²*, g_{KCa} = 0, g_{NaP} = g_{CAN} = 0), showing delayed excitation and a ramping firing rate due to slow inactivation of $I_{Kv1.2}$. The membrane potential exhibits an initial jump followed by gradual depolarization, leading to progressively increasing spike frequency.